Appendix A: Data File Formats

A number of file formats have been utilized for APT over the years (see [1] for additional examples). As the field continues to grow, new file and data standards may be required [2]. This appendix describes the file formats pertinent to LEAP.

The RRAW, STR, RHIT, and ROOT files have formats based on the ROOT software libraries provided by CERN [3]. These files contain binary objects that represent either data structures native to the ROOT system (such as histograms and graphs) or proprietary objects developed by CAMECA. The POS, ePOS, ATO, and range files are more readily interpretable by users, and their formats are described in detail below.

RRAW or STR Files (Raw Data)

RRAW files contain the raw detector data and the order of ion collection from the LEAP as well as the history of various parameters measured or controlled throughout the acquisition. Raw detector data consists of measurements of the time interval between the evaporation pulse (voltage or laser) and the detection of event pulses at either ends of multiple delay lines. The RRAW data is the primary input to the ion hit finding process and includes an entry for every evaporation pulse and any associated entries for event pulses. STR files replaced RRAW files in LEAP 4000 Systems starting in 2013 and contain the same information but in a modified format. General users do not interact with RRAW and STR files, but they can provide useful diagnostics to service personnel. For additional information on detection and hit finding see Chap. 3.

D.J. Larson et al., *Local Electrode Atom Probe Tomography: A User's Guide*,
DOI 10.1007/978-1-4614-8721-0, © Springer Science+Business Media New York 2013

RHIT Files (Hit Data)

RHIT files contain the nonzero entries of the RRAW or the STR file that meet certain quality criteria. These criteria collectively make up the algorithm known as hit finding. The RHIT file also contains other pertinent information for each event such as specimen voltage, pulse number, and temperature. An RHIT file contains a single interpretation of the hit finding of RRAW or STR data. If the hit finding criteria change, then alternative RHIT files could be generated.

ROOT Files (Reconstruction Data)

A ROOT file consists of a set of parameters used to convert the RHIT data into a specimen-space spatial reconstruction. Parameters included in the ROOT file include evaporation field, k factor, image compression factor, ion detection efficiency, atomic density, specimen shank angle, apex continuity relationships, as well as calibration factors used for conversion from time-of-flight spectra to mass-to-charge-ratio (m/n) spectra (see Chap. 5 for a detailed discussion of these parameters). In addition, histograms and graphs created as part of the calibration and reconstruction processing are stored for later reference. Unlike the RHIT and RRAW files which are generally created once per acquisition, multiple ROOT files may be created as per acquisition based on the specific parameters selected by the user: mass spectrum ranging definitions, the specific reconstruction algorithm, and individual reconstruction parameters. A ROOT file contains all of the parameters required to create POS or ATO files from an RHIT file.

POS Files (Position Data)

A POS file consists of the reconstructed ion positions and the m/n for each reconstructed ion as indicated in Table A.1. The POS file is created by applying the reconstruction algorithms specified in the ROOT files to the RHIT data and is the minimum set of information (with an appropriate range file described below) required to perform subsequent data analysis. This file type is typically used for

Table A.1 POS file record format

Data (4 × 4 bytes)			
Ion position (nm)			m/n
x	y	z	(Da)
Float	Float	Float	Float

higher level analysis (3D display, compositional analysis, creation of concentration profiles) and is the most widely used format for APT. The data for each of these fields are stored in the order of assignment from reconstruction as 4-byte IEEE Standard 754 single-precision floats in most-significant bit (big-endian) byte order. It should be noted that many systems read by least-significant bit order (small-endian) and that byte swapping may be required for successful interpretation outside of commercial CAMECA software.

RNG Files (Ranging Data)

Range files refer to files that describe a set of mass ranges associated with particular ion types. A range file applied to the *m*/*n* information in a POS file defines the elemental identity of each of the ions for 3D compositional analysis. Range files are ASCII (1 byte per character) format files that can be opened, read, and edited with many simple programs. At a minimum, they describe a lower limit and an upper limit to a range of bins in the *m*/*n* histogram that are identified with a specific ion type. Range files often include volume and color information as well. A hybrid version of a range file, the LAWATAP ENV file, includes instrument and reconstruction information [1].

An example RNG file is shown in Table A.2. The format originated from work at Oak Ridge National Laboratory [4] and the latest version includes fields defining ion color, lower/upper *m*/*n* limits, and composition (elemental or molecular). IVAS-generated RNG files are used with software developed for the LEAP instrument and may contain fields that are incompatible with the original format (ion descriptions with more than two characters and polyatomic ion for example). These incompatible items are stored after the last carriage return as a comments field that can be reincorporated into an RRNG file used in IVAS.

Each RNG file (Table A.2) begins with two integers that indicate the number of atom types and ion ranges (Line 1). Next, each 1–2-character atom type is followed by that same 1–2-character atom type and three values indicating the RGB color of the atom (Lines 2–10). Next, a table is included (Lines 10–19) which associates each ion *m*/*n* range (minimum and maximum value) with an integer combination of elements from the atom list in the first section (Lines 1–9). For example, Line 19 indicates that an ion with *m*/*n* between 71.5600 and 72.6640 Da is FeO (indicated by the entries of “1” under Fe and O and entries of “0” under Ni and H). After these required fields are additional fields added by IVAS to allow for proper translation into an RRNG format (see next section). In this example, the FeO ion is provided with a defined color (Lines 21–26).

Table A.2 RNG file example

Line								
1	4	9						
2	Fe							
3	Fe	1.00	0.00	1.00				
4	Ni							
5	Ni	0.00	0.80	0.00				
6	O							
7	O	0.00	0.80	1.00				
8	H							
9	H	0.80	0.80	0.00				
10	———————				Fe	Ni	O	H
11	.	53.6940	54.4660		1	0	0	0
12	.	55.6010	58.6890		1	0	0	0
13	.	59.6420	60.4820		0	1	0	0
14	.	60.6860	61.2080		0	1	0	0
15	.	61.6620	62.3430		0	1	0	0
16	.	63.7050	64.2280		0	1	0	0
17	.	15.9730	16.4960		0	0	1	0
18	.	0.9000	1.5590		0	0	0	1
19	.	71.5600	72.6640		1	0	1	0
20								
21	— polyatomic extension							
22	1	1						
23	FeO							
24	FeO	0.00	1.00	0.00				
25	——————————————————————— FeO							
26	.	71.5600	72.6640	1				

RRNG Files (Range Data)

An example RRNG file is shown in Table A.3. First, an ion section is defined (Lines 5–9) followed by range definitions (Lines 14–19). Each range includes the range minimum and maximum, ion volume, ion's atomic composition, and an optional color. Further descriptions of the required and optional fields are included within commented lines of the file itself.

ePOS Files (Extended Position Data)

The ePOS (or *extended* POS) file is the same headerless big-endian binary format as the POS file, but it includes additional four-byte columns describing detector information that enable more sophisticated analyses. The format detailed in Table A.4 includes ion position, *m*/*n*, far (uncorrected) time of flight, voltage, detector hit positions, and information on hit multiplicity. The extended information increases the file size but also expands the user's ability to analyze correlative

Table A.3 RRNG file example

Line	
1	# Comment lines can be included for any complete line entry; empty lines are also allowed.
2	# Ion and range sections must be properly identified with brackets [].
3	# Number identifier is required in each section to indicate the number of ion or range fields.
4	# Ion and range fields must follow Ion_Number and Range_Number formats.
5	[Ions]
6	Number = 3
7	Ion1 = Al
8	Ion2 = H
9	Ion3 = O
10	
11	# Range definitions require maximum and minimum range values.
12	# Mission vol: fields default to IVAS internal values.
13	# Color: field is optional.
14	Number = 7
15	Range1 = 13.3629 13.8335 vol:0.01661 Al:1 Color:33FFFF
16	Range2 = 26.7840 27.2700 vol:0.01661 Al:1 Color:33FFFF
17	Range3 = 28.9310 29.1160 vol:0.01661 Al:1 H:2 Color:FF0000
18	Range4 = 27.8820 28.1180 vol:0.00000 H:1 Color:CCCC00
19	Range5 = 0.9590 1.1720 vol:0.00000 H:1 Color:CCCC00
20	
21	# The Name: field is optional for giving ranges custom names.
22	# Custom ion names cannot be used to define ion types.
23	Range6 = 106.1250 213.4110 vol:0.00000 Name: Noise Color:0000FF
24	Range7 = 42.8160 43.3110 vol:0.04543 Al:1 O:1 Name: AlOLikely Color:00FFFF

evaporation (the spatial or the chemical influences on evaporation sequence) and perform alternate spatial reconstruction of the data.

Hit multiplicity is recorded in the last two columns of each record. When more than one ion is recorded for a given pulse, only the first event will have an entry in the "Pulses since last event pulse" column. Each subsequent event for that pulse will have an entry of zero because no additional pulser firings occurred before that event was recorded. Likewise, the "Ions Per Pulse" column will contain the total number of recorded ion events for a given pulse. This is normally one, but for a sequence of records for a pulse with multiply recorded ions, the first ion record will have the total number of ions measured in that pulse, while the remaining records for that pulse will have 0 for the Ions Per Pulse value.

ATO Files (Atom Files)

The ATO file format evolved to support TAP instrumentation and includes four major versions sharing the same ATO extension. The two contemporary versions are the version-three (V3) ATO which is associated with the LAWATAP instruments and the FlexTAP ATO format.

Table A.4 ePOS file record format

Data (11 × 4 bytes)										
Ion position (nm)			*m*/*n*	TOF	DC voltage	Pulse voltage	Detector position (nm)			
x	*y*	*z*	(Da)	(ns)	(kV)	(kV)	*X*	*Y*	Pulses since last event pulse	Ions per pulse
Float	Float	Float	Float	Float	Float	Float	Float	Float	Unsigned Int	Unsigned Int

Table A.5 ATO file record format (version 3)

Header (*8 × 1 byte*)													
NA	NA	NA	NA	Version	NA	NA	NA						
				3									
Data (*14 × 4 bytes*)													
Ion position (angstroms)			*m*/*n*	ClusterID	Pulse	DC voltage	TOF	Detector position (cm)		Pulse voltage (kV)	VVolt	FourierR	FourierI
x	*y*	*z*	(Da)		Number	(kV)	(μs)	*X*	*Y*				
Float	Float	Float	Float		Float	Float	Float	Float	Float	Float			

Table A.5 summarizes the LAWATAP V3 ATO file format. The first record is a header with subsequent records containing information about individual ions. Each record is stored in big-endian format. The header consists of eight 1-byte entries where the fifth entry contains the value 0x03. The data section of the file consists of 56-byte fixed-length records recorded in acquisition order. The fourteen 4-byte floating point columns include ion position, m/n, pulse number, voltage, time of flight, and detector hit position. Additional fields exist but are not defined for use with IVAS software. It is worthy to note that the pulse number is a 32-bit floating-point binary, and unless it is reset to zero every 2^{24} (~16.7 million) pulses (as is typical for the LAWATAP system) it will lose precision as modern datasets typically contain additional pulse events.

The FlexTAP version ATO file is similar to a tagged image file format (TIFF) and contains a 16-byte header followed by a table describing the tags. FlexTAP ATO files are converted automatically to RHIT files after acquisition of data from a FlexTAP instrument.

References

1. Gault, B., Moody, M.P., Cairney, J.M., Ringer, S.P.: Atom Probe Microscopy. Springer Series in Materials Science, vol. 160. Springer (2012)
2. Miller, M.K.: Proposed XML-based three-dimensional atom probe data standard. Surf. Interface Anal. **36**(5–6), 601–605 (2004)
3. Brun, R., Rademakers, F.: ROOT - an object oriented data analysis framework. Nucl Instrum. Meth. Phys. Res. A **389**, 81–86 (1997)
4. Miller, M.K.: The ORNL atom probe software package. J. Phys. **47**-**C2**(3), 499–504 (1986)

Appendix B: Field Evaporation

Field *ionization* is the physical mechanism that makes field-ion microscopy possible. Field *evaporation* is the physical mechanism that makes atom-probe analysis possible. These processes are introduced below, but it is important to note that the theories to describe these processes are still early in their development, even after 60 years.

Field Ionization and Field-Ion Microscopy

After Müller demonstrated experimental evidence of field ionization using the FIM in 1951 [1], a theoretical explanation was initiated and developed by Inghram and Gomer [2] and was continued by Müller and Bahadur [3]. In field-ion microscopy, imaging gas atoms in the vicinity of the specimen undergo field ionization. Due to an applied voltage on the specimen, the gas atoms are attracted to the sample surface by an induced dipole force [4]. The gas atoms impact the specimen and rebound from the surface, losing a portion of their kinetic energy. This process occurs repeatedly until the gas atom is ionized by the high field directly above the most protruding atoms. During ionization, the gas atom's topmost electron tunnels into the sample surface, and the gas ion is then accelerated away from the specimen by the electric field (typically of strength $\geq$20 V/nm).

Ionization occurs because the potential-energy barrier for the topmost electron is reduced both by the applied field and by interactions with the specimen surface [5]. The highest probability of tunneling occurs at a distance of ~0.2–0.5 nm above the specimen and is greatest in the high-field regions directly above the nuclei of protruding specimen atoms. Because the gas atoms are preferentially ionized at these positions, an image is obtained which shows the protruding surface atoms as bright spots. Thus, an FIM image maps the high-electric-field locations above a specimen surface. The emission current density is determined both by the tunneling rate constant and by gas-distribution effects that influence the probability that a gas atom is in the right place to be ionized [6, 7].

D.J. Larson et al., *Local Electrode Atom Probe Tomography: A User's Guide*,
DOI 10.1007/978-1-4614-8721-0, © Springer Science+Business Media New York 2013

Introduction to Field Evaporation

Field evaporation (FEV) is the removal of *specimen* atoms, in the form of ions, from a surface, as result of applying a very high electric field. This is in contrast to adsorbate field desorption, which is closely related to field evaporation and refers to the removal of adsorbed *foreign* atoms from the specimen surface. The two processes are basically the same from a theoretical standpoint.

FEV is sometimes a two-stage process, involving first the *escape* of an atom into an *escape charge state n* (i.e., its charge is *ne*, where *e* is the elementary positive charge), and then *post-field ionization* of the ion, in one or more steps, to a higher final charge state. The escape step is normally taken to be thermal activation over a barrier of height Q_n, with *FEV rate constant* $k_n(F,T)$ given by

$$k_n(F,T) = A\exp[-Q_n(F)/k_B T], \tag{B.1}$$

where F is the *atom-probe* (*AP*) *operating field* (as applied to surface atoms that are *at high risk* of FEV), T is the thermodynamic temperature, k_B is the Boltzmann constant, and A is the *rate constant pre-factor* (often taken as equal to the surface-atom vibration frequency). The rate constant k_n is measured in s^{-1}. If n_{hr} denotes the count of specimen surface atoms, within the AP detector's field of view, that are at high risk of FEV, then the effective operating flux (or rate) R during FEV is given by the *FEV emission equation*

$$R = n_{hr}k_n(F,T) = \{n_{hr}A\}\exp[-Q_n(F)/k_B T]. \tag{B.2}$$

The value of n_{hr} is not well established, but is sometimes taken as 0.01 layers or 100 atoms. The flux or rate R is measured in layers/s, atoms/s, or ions/s.

In principle, two parameters in basic FEV theory are particularly important for atom-probe operation: (a) the *zero-barrier evaporation field* (ZBEF) F^E, which is the operating field at which Q_n becomes equal to zero, and (b) the field sensitivity dQ_n/dF, for F-values near F^E. Practical operating-field values depend both on the chosen (but often not well known) operating flux and on emitter temperature (which is usually not well known for laser pulsed AP). Consequently, practical F-values are not themselves well known. However, in principle they must be slightly or somewhat less than the ZBEF. Hence, a theoretical estimate of the ZBEF can be used as a first estimate of the AP operating field. Theoretical ZBEF estimates can be derived from an atomic-level version of the principle of conservation of energy, as below.

Knowledge of the field sensitivity dQ_n/dF, near F^E, is needed if it is wished to predict how, for given flux R, the corresponding operating field F_R varies with temperature T, and consequently how the fractional field reduction (FR%) varies with temperature. This information is important for correct AP operation. To derive dQ_n/dF, it is necessary to know how Q_n varies with F, near F^E. This, in turn, requires that a reliable physical model of the FEV escape process be available.

In the early days of field-ion microscopy, it was assumed that FEV could be described by the classical image-hump model [8] (for reviews, see [9, 10]), but tests have repeatedly shown that this model is unable to accurately describe experimental data relating to field sensitivity (e.g., [11]). Hence, it came to be thought that escape takes place via some form of charge-exchange mechanism [12, 13], in which escape and ionization take place simultaneously at/near the top of an activation-energy hump.

It is now believed [14] that FEV escape takes place by a particular form of charge-exchange, termed the "revised charge-draining mechanism." In this, FEV is described as the evaporation of a partial-ion, in a partially charged state, over a charge-draining hump. (A partial-ion is an atom that does not have an integral number of electrons in the region of space associated with the atom. Gauss' theorem implies that atoms at highly charged surfaces must behave like this.)

Charge-draining is an intrinsically quantum-mechanical (QM) phenomenon. Hence, $Q_n(F)$ can be reliably determined only by QM calculations. In the high-field situation of the AP, it is intensely difficult to make such calculations fully reliable. Useful FEV calculations have been performed only for tungsten (e.g., [15]) and (perhaps) for aluminum [16]. Consequently, for most materials, data relating to fractional field reduction needs to be acquired via experiment.

The Prediction of Zero-Barrier Evaporation Field

Simple (approximate) ZBEF prediction can be carried out using the following more general mathematics. First, obtain an expression for the potential energy (PE) of an n+ ion, measured relative to the energy level of the base of the partial-ion's bonding well. This PE can be denoted by $W_n(x, F)$, where x is the distance of the ion nucleus from the specimen's electrical surface. (The electrical surface is near the outer edge of the surface-atom electron charge clouds.) The FEV activation energy is then given by $Q_n(F) = W_n(x^{\mathrm{e}}, F)$, where the "escape distance" x^{e} is the distance of the top of the activation-energy hump from the specimen's electrical surface and is a function of operating field F. The zero-activation-energy condition is then expressed as

$$Q_n\left(F^{\mathrm{E}}\right) = W_n\left(x^{\mathrm{e}0}, F^{\mathrm{E}}\right) = 0, \tag{B.3}$$

where $x^{\mathrm{e}0}$ is the "zero-barrier escape distance," i.e., the escape distance corresponding to the condition $Q_n = 0$. The resulting expression, sometimes called an "energy-balance equation," contains three variables $\{n, x^{\mathrm{e}0}, F^{\mathrm{E}}\}$. This equation is then solved for F^{E}, using auxiliary methods to determine values for $x^{\mathrm{e}0}$ and n, as described below.

The mathematics just set out is general: the main approximation comes in finding a suitable simple expression for $W_n(x, F)$. This can be done using three

physical steps. First, calculate the "local zero-field activation energy" (Q_{0n}) needed to create an n+ ion at a position x "somewhat" outside a defined part of the surface, outside the reach of all short-range ion-surface interactions, in the absence of any applied field. This is done by the following formal cycle. (1) Remove the bound surface "atom" to become a neutral atom in remote field-free space: assume this takes work Λ^0, where Λ^0 is the zero-field bonding energy of the atom, normally taken equal to the tabulated sublimation energy. (2) Remove n electrons from the neutral atom, one by one, leaving them in remote field-free space, well separated from each other and from the resulting ion: this takes work H_n equal to the sum of the first n ionization energies of the atom. (3) Take the electrons, one-by-one, to the emitter Fermi level, via paths that all pass through the position x "somewhat" outside the surface, and then move the ion to position x: in this combined process, an amount of energy $n\phi$ is retrieved, where ϕ is the local work function of the part of the specimen surface that faces the external ion. It follows that

$$Q_{0n} = \Lambda^0 + H_n - n\phi = \Lambda^0 + \sum_{s=1}^{n} I_s - n\phi, \tag{B.4}$$

where I_s is the sth ionization energy. This quantity Q_{0n} is not really an activation energy as usually defined, hence it is sometimes called the "thermodynamic term" and denoted by ${K_n}^0$.

In the second step, move the ion closer to the surface, to a new position x within the range of attractive ion-surface forces but outside the range of short-range repulsive forces, and assume (somewhat arbitrarily and not necessarily correctly) that the strongest attractive force is due to image forces. This step introduces an image-PE contribution $-n^2e^2/16\pi\varepsilon_0 x$, where ε_0 is the electric constant. In the third step, apply an electric field of mean strength F: this introduces an electrostatic PE contribution $-neFx$. The final (approximate) expression for $W_n(x, F)$ is

$$W_n(x, F) = Q_{0n} - neFx - n^2e^2/16\pi\varepsilon_0 x \tag{B.5}$$

and the corresponding (approximate) energy-balance equation is

$$Q_{0n} - neF^{\mathrm{E}}x^{\mathrm{e}0} - n^2e^2/16\pi\varepsilon_0 x^{\mathrm{e}0} = 0. \tag{B.6}$$

Now ask what is the maximum field ${F_n}^{\mathrm{M}}$ that (for a given value of n) can be predicted from this equation. Applying the condition $\mathrm{d}F^{\mathrm{E}}/\mathrm{d}x^{\mathrm{e}0} = 0$ finds the maximum field as

$$F_n^{\mathrm{M}} = \left(4\pi\varepsilon_0/n^3e^3\right)\left(Q_{0n}\right)^2 \cong \left(0.6944616\,\mathrm{V\,nm^{-1}\,eV^{-2}}\right)\left(Q_{0n}\right)^2/n^3. \tag{B.7}$$

This field corresponds to an escape distance ${x_n}^{\mathrm{M}}$ given by

$$x_n^{\mathrm{M}} = \left(ne/16\pi\varepsilon_0 F_n^{\mathrm{M}}\right)^{1/2} = 2n^2e^2/16\pi\varepsilon_0 Q_{0n}. \tag{B.8}$$

Equation (B.7) has been called *Müller's formula*, because a formula of this type (albeit incorrect in detail) was first given by Müller [8]. (In fact, both Gomer and Swanson [13] and Brandon [17] contributed to giving the correct Müller-type formula for an *n*+ ion.) Correspondingly, $F_n{}^{\mathrm{M}}$ can be called the *Müller escape field* for an *n*+ ion, and $x_n{}^{\mathrm{M}}$ the *Müller escape distance* for an *n*+ ion.

Evaluation of values for $x_n{}^{\mathrm{M}}$ suggests that, for many species, the distance $x_n{}^{\mathrm{M}}$ is noticeably different from estimates (made in other ways) of the distance x^{b} of the base of the bonding well from the specimen's electrical surface. (In particular, when $x_n{}^{\mathrm{M}} < x^{\mathrm{b}}$, the calculation cannot be physically realistic, because strong repulsive forces are being ignored.) Physically, one expects the position of the base of the bonding well to be the main factor that influences where escape occurs. Hence, it is better in principle to set $x^{\mathrm{e}0} = x^{\mathrm{b}}$, and rearrange (B.6) into the form

$$F_n^{\mathrm{E}}\left(x^{\mathrm{b}}\right) = \left(Q_{0n} - n^2e^2/16\pi\varepsilon_0 x^{\mathrm{b}}\right)/nex^{\mathrm{b}}. \tag{B.9}$$

This formula, introduced by Tsong [18], was used by Müller and Tsong for their systematic 1969 calculations [19], in which they set x^{b} equal to the Pauling atomic radius [20] for the element of interest.

Equation (B.9) can also be used to define a correction factor $\gamma_n(x^{\mathrm{b}})$ by

$$F_n^{\mathrm{E}}\left(x^{\mathrm{b}}\right) = \gamma_n\left(x^{\mathrm{b}}\right) \times F_n^{\mathrm{M}}. \tag{B.10}$$

It has been shown [21] that $\gamma_n(x)$ is a slowly varying function of distance; explicitly, calculations for 55 elements (Forbes, unpublished work) have shown that for many elements $\gamma_n(x^{\mathrm{b}})$ is in the range: $0.90 \leq \gamma_n(x^{\mathrm{b}}) \leq 1$. Consequently, for a charge-exchange-type model, the numerical value of $F_n{}^{\mathrm{M}}$ can be used as a satisfactory estimate for $F_n^{\mathrm{E}}\left(x^{\mathrm{b}}\right)$. Values of $F_n{}^{\mathrm{M}}$ were first systematically calculated by Tsong [22] and are tabulated in many AP textbooks, usually for $n = 1, 2, 3$.

The value of the parameter $F_n^{\mathrm{E}}\left(x^{\mathrm{b}}\right)$ depends on *n*. *Brandon's criterion* [17] is to take the lowest of these values as the theoretical estimate of zero-barrier evaporation field F^{E}, and the corresponding value of *n* as the theoretically predicted escape charge state. Elementary FEV theory (as found in APT textbooks) normally uses the *Müller-Brandon approach*, in which ZBEF estimates are obtained by applying Brandon's criterion to the Müller escape fields as determined above.

Note that the derivation of Müller's formula given above relates primarily to the energetics of the escape process, does not involve the assumption that escape takes place via the classical image-hump mechanism, but does show that Müller's formula is applicable (as an approximation) to charge-exchange-type escape mechanisms [14, 21].

Müller's formula was originally derived mathematically in a different way, by assuming that escape takes place via the classical image-hump mechanism, and was originally called the "image-hump formula." The continued use of this name is unfortunate, because it can give the spurious (logically false) impression that the success of Müller's formula justifies the use of the image-hump (IH) model in the

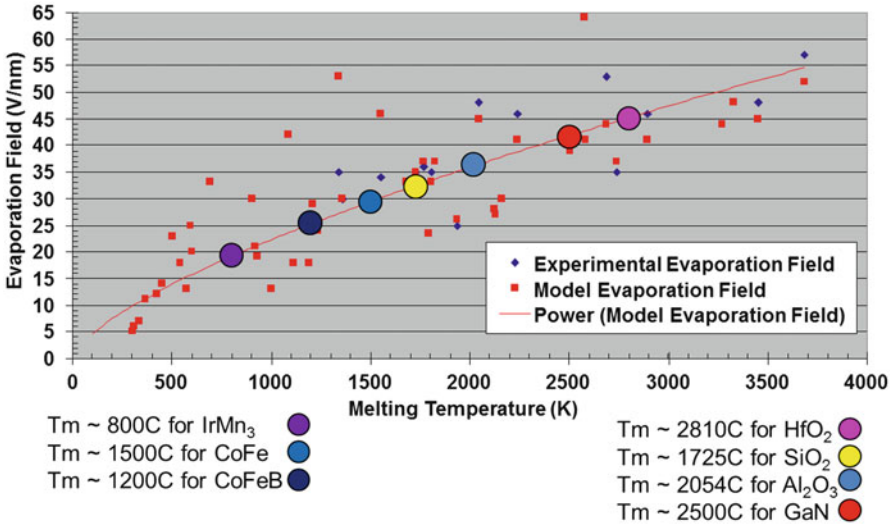

Fig. B.1 The melting temperature of various elements versus their theoretical and experimentally determined evaporation fields. This chart allows a *zeroth-order* estimate of the evaporation field for an element or compound if one is unavailable from the Müller-Brandon approach

context of field sensitivity, whereas the facts of the matter are that the IH-model field-sensitivity predictions have failed badly (quantitatively) on almost every occasion in the last 70 years on which they have been seriously tested. There can also be a spurious (logically false) conclusion that because the image-hump model fails badly, the so-called "image-hump formula" is not useful. In order to avoid both these types of false impression/conclusion, the name "Müller's formula" is to be preferred. However, it does need to be emphasized that the Müller-Brandon approach estimates the ZBEF and that it is an approximation. For many materials, Müller's formula appears to be satisfactory as a simple first approximation, but we do not currently know how good it is. Significant work remains to develop a theory of FEV escape that is predictive and applicable for both metals and nonmetals in both laser and voltage pulse modes.

If the user desires an estimate of an evaporation field for an element or compound, a zeroth-order estimate may be obtained by plotting the melting temperature of various elements versus their theoretical and experimentally determined evaporation field as shown in Fig. B.1. Although there is significant scatter in the phenomenological power law fit ($R^2 \sim 0.7$) shown on the plot, this method may provide at least a starting point for the evaporation field if such a value is unavailable. It is clear that for compounds such an estimate will be more accurate for miscible alloys as opposed to ordered phases.

Field Evaporation Charge States and Post-field-ionization

The Müller-Brandon approach, as described above and as implemented by Tsong [22], predicts that most materials will escape in a singly charged or doubly charged state (with a few of the most refractory metals predicted to escape as 3+ ions). Although there are individual exceptions, this prediction does agree surprisingly well with many experimental FEV results, for the low-temperature cases where the activation energy Q_n has to be very low [5, 10]. However, in some cases, higher charge states are found (as high as 6+ for tungsten at very high fields [23]). Following definitive experimental work by Ernst [24], it is now generally accepted that these higher charge states are formed by a process called *post-field-ionization* (PFI) (or simply "post-ionization"), in accordance with a theory developed by Haydock and Kingham [25, 26].

For PFI to occur, it is necessary both for the energetics to be right and for the probability of PFI to be high enough. Examination of the ionic PE expression, (B.5), shows that as x gets large, the energy curves for high charge-state values must eventually cross those for lower charge-state values [9]. This implies that escaping ions can be post-field-ionized at some distance from the specimen surface. Kingham has concluded that it is likely that, for most (probably all) metals, PFI can occur and field evaporation can be a multi-stage process. He has performed calculations predicting charge state as a function of applied field for a large number of elements [5]. These curves can also be found in APT textbooks (e.g., [10, 27]).

Comparisons of theory and experiment, for how charge state varies with operating field, show good agreement for many metals. In suitable cases, where a species is found to field evaporate in two adjacent charge states, and one can be reasonably sure that the higher charge state is formed by PFI, measurements of the counts of ions in the two charge states can, via the Kingham diagrams, be used to estimate the field over the part of the emitter that generates the measured ion counts.

Field Evaporation Induced by Laser or Electron Pulses

From the above discussion it is clear that the rate of field evaporation can be enhanced simply by increasing the applied field on the specimen. Field evaporation may also be significantly enhanced by irradiation of the specimen by a beam of photons or electrons. It is exactly this effect that provides the operating mechanism for the pulsed-laser atom probe [28]. Tsong [5] proposed that the enhancement in field evaporation could be caused by two effects. The first, and simplest, effect is emitter heating by the particle beam. The inelastic interaction of the particles with the emitter produces a temperature rise in the specimen, and hence an increase in the FEV rate constant in accordance with (B.1). With a reliable model for $Q(F)$ (or reliable empirical data for the FEV operating flux in use), the change in the field evaporation characteristics could be calculated.

The second possibility is a direct particle-induced electronic excitation. An incoming particle (photon or electron) will have a probability of exciting an electron of a specimen surface atom to a higher energy state (thereby allowing field ionization from this excited state) or of ionizing the atom directly. If this occurs for a metal atom, the ion would usually be quickly re-neutralized as a result of electron transfer from an energy level in the metal conduction band [5], because the filled conduction-band levels in the metal are higher than the energy level of the electron that was ejected to form the ion.

Tsong has found no effect of direct electronic excitations by photons in pulsed-laser stimulated field desorption from metal surfaces if the photon intensity is not excessively high [5]. This result was deduced by comparing the energy distributions of pulsed-laser field desorbed ions with those found in ordinary field desorption. An excess energy tail, or a separate peak, is evidence of direct excitation of the surface atom by incoming particles before evaporation occurs. It should be noted, however, that if the laser power is very intense, an excess energy can be detected irrespective of whether the specimen is nonmetallic [5].

Work continues on understanding photon/specimen interactions, but current understanding is that the dominant effect is as follows. The laser energy creates a very brief rise in specimen temperature for both metals and nonmetals, thereby inducing field evaporation [29]. The existence of different specimen cooling times (as a result of differences in shape and/or thermal conduction properties) seems to be the main reason why different specimens demonstrate differences in mass resolving power [30].

We thank Dr. Richard G. Forbes for assistance with the preparation of this Appendix.

References

1. Müller, E.W.: Z. Phys. **131**, 136–142 (1951)
2. Inghram, M.G., Gomer, R.: Mass spectrometric analysis of ions from the field microscope. J. Chem. Phys. **22**, 1279–1280 (1954)
3. Müller, E.W., Bahadur, K.: Field ionization of gases at a metal surface and the resolution of the field ion microscope. Phys. Rev. **102**(3), 624–634 (1956)
4. Tsong, T.T., Muller, E.W.: Field adsorption of inert-gas atoms on field ion emitter surfaces. Phys. Rev. Lett. **25**(14), 911–913 (1970)
5. Tsong, T.T.: Atom-Probe Field Ion Microscopy: Field Ion Emission and Surfaces and Interfaces at Atomic Resolution. Cambridge University Press, Cambridge, UK (1990)
6. Forbes, R.G.: Seeing atoms: the origins of local contrast in field ion images. J. Phys. Appl. Phys **18**, 973–1018 (1985)
7. Forbes, R.G.: Field ion imaging old and new. Appl. Surf. Sci. **94/95**, 1–16 (1996)
8. Müller, E.W.: Field desorption. Phys. Rev. **102**, 618–624 (1956)
9. Miller, M.K., Smith, G.D.W.: Atom Probe Microanalysis: Principles and Applications to Materials Problems. Materials Research Society, Pittsburgh, PA (1989)

10. Miller, M.K., Cerezo, A., Hetherington, M.G., Smith, G.D.W.: Atom Probe Field Ion Microscopy. Oxford University Press, Oxford (1996)
11. Forbes, R.G., Biswas, R.K., Chibane, K.: Field evaporation theory: a re-analysis of published field sensitivity data. Surf. Sci. **114**, 498–514 (1982)
12. Gomer, R.: Field desorption. J. Chem. Phys. **31**, 341–345 (1959)
13. Gomer, R., Swanson, L.W.: Theory of field desorption. J. Chem. Phys. **38**, 1613–1629 (1963)
14. Forbes, R.G.: Field evaporation theory: a review of basic ideas. Appl. Surf. Sci. **87**, 1–11 (1995)
15. Wang, L.C., Kreuzer, H.J.: Kinetic theory of field evaporation of metals. Surf. Sci. **237**, 337–346 (1990)
16. Sánchez, C.G., Lozovoi, A. Y., Alavi, A. Field evaporation from first principles. Mol. Phys. **102**, 1045–1055 (2004)
17. Brandon, D.G.: The structure of field-evaporated surfaces. Surf. Sci. **3**, 1–18 (1964)
18. Tsong, T.T.: On the mechanism of field evaporation. Surf. Sci. **10**, 102–117 (1968)
19. Müller, E. W., Tsong, T.T.: Field Ion Microscopy: Principles and Applications. Elsevier, New York, NY, 1969
20. Pauling, L.: The Nature of the Chemical Bond. Cornell University Press, Ithaca, NY, 1960
21. Forbes, R.G.: A new formula for predicting low temperature evaporation field. Appl. Phys. Lett. **40**, 277–279 (1982)
22. Tsong, T.T.: Field ion image formation. Surf. Sci. **70**, 211–233 (1978)
23. Müller, E.W., Krishnaswamy, S.V.: High ion charges in field-evaporating 5*d* transition metals. Phys. Rev. Lett. **37**, 1011–1014 (1976)
24. Ernst, N: Experimental investigation on field evaporation of singly and doubly charged rhodium. Surf. Sci. 87 469–482 (1979)
25. Haydock, R., Kingham, D.R.: Post-ionization of field-evaporated ions. Phys. Rev. Lett. **44**, 1520–1523 (1980)
26. Kingham, D.R.: The post-ionization of field evaporated ions: a theoretical explanation of multiple charge states. Surf. Sci. **116**, 273–301 (1982)
27. Gault, B, Moody, M.P., Cairney, J.M., Ringer S.P.: Atom Probe Microscopy. Springer, New York, NY, 2012
28. Kellogg, G.L., Tsong, T.T.: Pulsed-laser atom-probe field-ion microscopy. J. Appl. Phys. **51**(2), 1184–1194 (1980)
29. Bunton, J.H., Olson, J.D., Lenz, D., R., Kelly, T.F.: Advances in pulsed-laser atom probe: instrument and specimen design for optimum performance. Microsc. Microanal. **13**, 418–427 (2007)
30. Vella, A., Mazumder, B., Da Costa, G., Deconihout, B.: Field evaporation mechanism of bulk oxides under ultra fast laser illumination. J. Appl. Phys. **110**, 044321 (2011)

Appendix C: Reconstruction Geometry

Overview

In this appendix several geometric exercises are used to illustrate the definitions essential for spatial reconstructions by using and building on approaches previously established in the literature [1–4]. We start by defining common terms that are relied upon later, and then calculations are developed for the lateral projection and the volume increment. We finish by showing a calculation of the shank angle from the voltage curve. In all of these calculations the apex is assumed to be spherical and situated on a conical shank. We try to follow the convention that distances on the scale of the whole instrument will be in upper case (flight path L_{Det} for example) while local properties of the tip will be in lower case (r_{Tip} for example).

Image Compression

The projection model is illustrated in Fig. C.1 and assumes that a single projection point exists at a distance mr_{Tip} beyond the center of the spherical apex, where $\xi = 1 + m$ is known as the image compression factor. Assuming that an ion is launched normal to the sphere surface (with angle θ_{Launch}), the effect of ξ is to reduce the projection angle to θ_{Det} and with it the magnification.

The reconstruction process is the task of transforming a detector position into a launch position on the tip, r_{Launch}. By considering the detector/flight path triangle, we know the compressed angle:

$$\cos\left(\theta_{\mathrm{Det}}\right) = \frac{L_{\mathrm{Det}}}{\sqrt{L_{\mathrm{Det}}^2 + R_{\mathrm{Det}}^2}} \quad \text{and} \quad \sin\left(\theta_{\mathrm{Det}}\right) = \frac{R_{\mathrm{Det}}}{\sqrt{L_{\mathrm{Det}}^2 + R_{\mathrm{Det}}^2}}. \tag{C.1}$$

D.J. Larson et al., *Local Electrode Atom Probe Tomography: A User's Guide*,
DOI 10.1007/978-1-4614-8721-0, © Springer Science+Business Media New York 2013

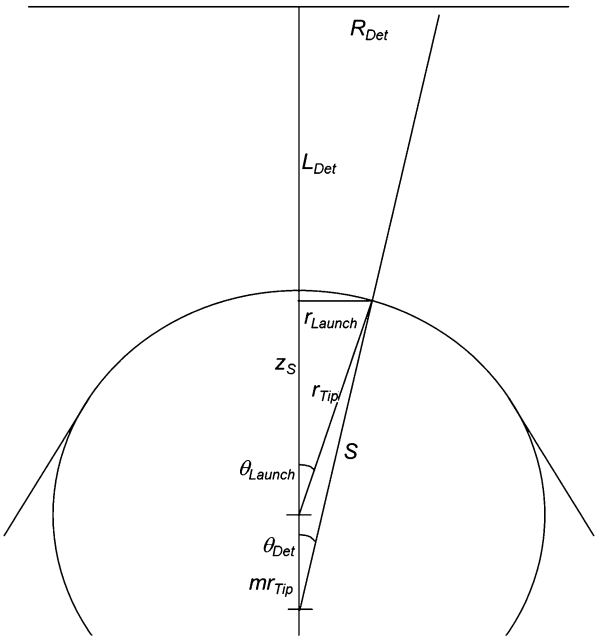

Fig. C.1 Tip geometry relevant for image compression

We will approach this by trying to solve for

$$\tan(\theta_{\text{Launch}}) = \frac{r_{\text{Launch}}}{z_{\text{S}}}. \tag{C.2}$$

We start by looking at r_{Launch}, inside the tip:

$$\sin(\theta_{\text{Det}}) = \frac{r_{\text{Launch}}}{s} \tag{C.3}$$

s can be computed using the law of cosines and writing:

$$r_{\text{Tip}}^2 = m^2 r_{\text{Tip}}^2 + s^2 - 2mr_{\text{Tip}} s\cos(\theta_{\text{Det}}).$$

Gathering s terms on the left we get

$$s^2 - 2mr_{\text{Tip}} s\cos(\theta_{\text{Det}}) = r_{\text{Tip}}^2 - m^2 r_{\text{Tip}}^2.$$

Completing the square gives us

$$s^2 - 2mr_{\text{Tip}} s\cos(\theta_{\text{Det}}) + m^2 r_{\text{Tip}}^2 \cos^2(\theta_{\text{Det}}) = r_{\text{Tip}}^2 - m^2 r_{\text{Tip}}^2 + m^2 r_{\text{Tip}}^2 \cos^2(\theta_{\text{Det}})$$

and we find

$$s = r_{\text{Tip}}\left(m\cos\left(\theta_{\text{Det}}\right) + \sqrt{1 - m^2\sin^2(\theta_{\text{Det}})}\right).$$

Because it will be useful to us later we define

$$\gamma = m\cos\left(\theta_{\text{Det}}\right) + \sqrt{1 - m^2\sin^2(\theta_{\text{Det}})} \tag{C.4}$$

and we write

$$s = \gamma r_{\text{Tip}} \tag{C.5}$$

$$r_{\text{Launch}} = \gamma r_{\text{Tip}}\sin\left(\theta_{\text{Det}}\right). \tag{C.6}$$

Using the Pythagorean theorem we can write

$$\left(z_{\text{S}} + m r_{\text{Tip}}\right)^2 + r_{\text{Launch}}^2 = s^2$$

Substituting in our expressions for s and r_{Launch} we find

$$z_{\text{S}} = r_{\text{Tip}}(\gamma\cos\left(\theta_{\text{Det}}\right) - m) \tag{C.7}$$

so substituting (C.6) and (C.7) back into (C.2) we obtain

$$\tan\left(\theta_{\text{Launch}}\right) = \frac{\gamma\sin\left(\theta_{\text{Det}}\right)}{\gamma\cos\left(\theta_{\text{Det}}\right) - m}. \tag{C.8}$$

To evaluate the small-angle limit of this expression we will substitute back in for the definition of γ to write

$$\tan\left(\theta_{\text{Launch}}\right) = \frac{m\sin\left(\theta_{\text{Det}}\right)\cos\left(\theta_{\text{Det}}\right) + \sin\left(\theta_{\text{Det}}\right)\sqrt{1 - m^2\sin^2(\theta_{\text{Det}})}}{m\sin^2(\theta_{\text{Det}}) + \cos\left(\theta_{\text{Det}}\right)\sqrt{1 - m^2\sin^2(\theta_{\text{Det}})}}.$$

We make the approximations $\sin\left(\theta_{\text{Det}}\right) = \theta_{\text{Det}}$ and $\cos\left(\theta_{\text{Det}}\right) = 1$. Noting that we have a term proportional to unity in the denominator but must keep θ_{Det} to first order in the numerator we get

$$\tan\left(\theta_{\text{Launch}}\right) = \frac{(m+1)\theta_{\text{Det}}}{1}.$$

With a small-angle limit on the (larger) launch angle this reduces to the useful approximation

$$\theta_{\text{Launch}} = \xi\theta_{\text{Det}}. \tag{C.9}$$

Lateral Magnification

In developing our expression for the compressed trajectory we found (C.6). This equation is very important in itself as it relates the position on the detector to the radial launch position on the tip. So we will go back to (C.1)–(C.3) in order to evaluate the ratio $R_{\mathrm{Det}}/r_{\mathrm{Launch}}$.

$$r_{\mathrm{Launch}} = \frac{sR_{\mathrm{Det}}}{\sqrt{L_{\mathrm{Det}}^2 + R_{\mathrm{Det}}^2}}$$

and then

$$r_{\mathrm{Launch}} = \frac{sR_{\mathrm{Det}}\cos\left(\theta_{\mathrm{Det}}\right)}{L_{\mathrm{Det}}}.$$

So our expression for magnification is

$$\eta = \frac{R_{\mathrm{Det}}}{r_{\mathrm{Launch}}} = \frac{L_{\mathrm{Det}}}{s\cos\left(\theta_{\mathrm{Det}}\right)} = \frac{L_{\mathrm{Det}}}{\gamma\cos\left(\theta_{\mathrm{Det}}\right)r_{\mathrm{Tip}}}.$$

This is the expression that applies to large field of view (FOV) local electrode atom probes. In order to obtain the classical small FOV expression for lateral magnification we take the small-angle limits for s and $\cos(\theta_{\mathrm{Det}})$ to get

$$r_{\mathrm{Launch}} = \frac{\xi R_{\mathrm{Det}} r_{\mathrm{Tip}}}{L_{\mathrm{Det}}}$$

so the small-angle magnification is

$$\eta = \frac{R_{\mathrm{Det}}}{r_{\mathrm{Launch}}} = \frac{L_{\mathrm{Det}}}{\xi r_{\mathrm{Tip}}}. \tag{C.10}$$

Variation of Tip Radius with Analysis Depth

The radius of the apex is a key component in understanding all aspects of the spatial reconstruction. It is important to both the radial magnification as well as the depth increment per atom. As shown in Fig. C.2, we start with the simple case where the sphere of the apex and the cone of the shank meet with tangential continuity.

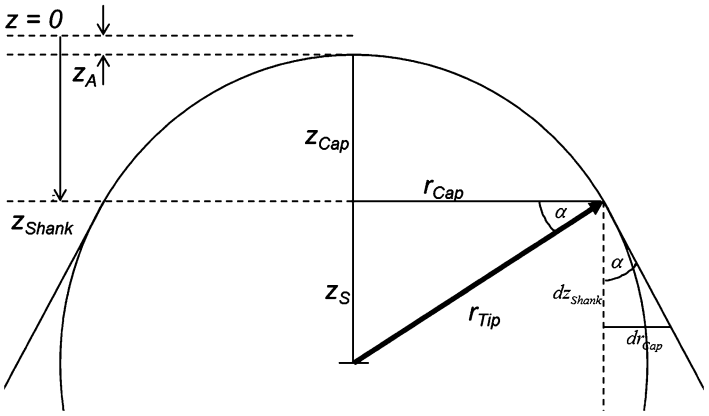

Fig. C.2 Tip geometry for variation of tip radius as a function of analysis depth and tangential continuity

Tangentially Continuous Case

We begin by writing down the expected variation of tip radius with analysis depth for a fixed shank half-angle, α. Note that the angle α describes how the radius of the spherical cap varies with the depth of the sphere–cone intersection:

$$\frac{\mathrm{d}r_{\mathrm{Cap}}}{\mathrm{d}z_{\mathrm{Shank}}} = \tan(\alpha). \tag{C.11}$$

We are trying to evaluate how the apex radius varies with analysis depth, z_{A}:

$$\frac{\mathrm{d}r_{\mathrm{Tip}}}{\mathrm{d}z_{\mathrm{A}}} \equiv K_{\alpha}. \tag{C.12}$$

Just by looking at our definitions, we can write $z_{\mathrm{A}} = z_{\mathrm{Shank}} - z_{\mathrm{Cap}}$ and $z_{\mathrm{Cap}} = r_{\mathrm{Tip}} - z_{\mathrm{S}}$. By looking at the triangle including the sphere center we can see $z_{\mathrm{S}} = r_{\mathrm{Tip}} \sin(\alpha)$. Substituting into the definition of z_{A} we get

$$z_{\mathrm{A}} = z_{\mathrm{Shank}} + r_{\mathrm{Tip}}(\sin(\alpha) - 1). \tag{C.13}$$

We want the derivative of z_{A}, so we get ready by finding the derivative of z_{Shank} first. Again from the central triangle we have

$$\frac{r_{\mathrm{Cap}}}{r_{\mathrm{Tip}}} = \cos(\alpha)$$

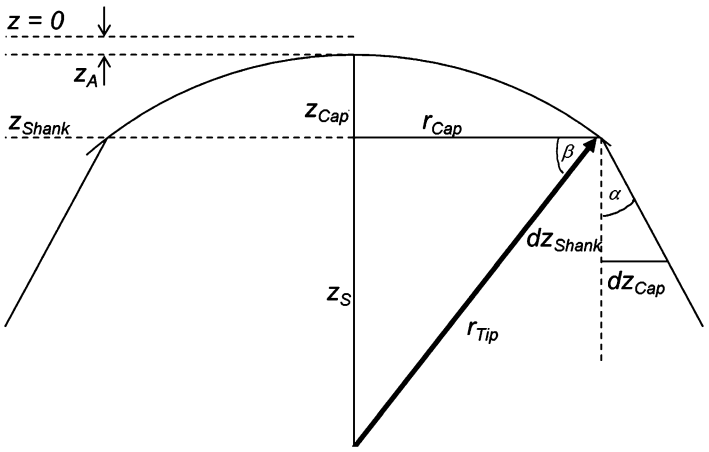

Fig. C.3 Tip geometry for variation of tip radius as a function of analysis depth without tangential continuity

which we can substitute into our definition of tan (α) to see

$$\frac{\mathrm{d}z_{\mathrm{Shank}}}{\mathrm{d}r_{\mathrm{Tip}}} = \frac{\cos(\alpha)}{\tan(\alpha)}.$$

So now we just take the derivative of the analysis depth to obtain

$$\frac{\mathrm{d}z_{\mathrm{A}}}{\mathrm{d}r_{\mathrm{Tip}}} = \frac{\cos(\alpha)}{\tan(\alpha)} + \sin(\alpha) - 1$$

Just simplifying, this gives us [1]

$$K_{\alpha} = \frac{\sin(\alpha)}{1 - \sin(\alpha)}. \tag{C.14}$$

Non-tangentially Continuous Case

In this more general specimen geometry shown in Fig. C.3, we relax the requirement that the apex meets smoothly with the shank. We hold that the tip radius r_{Tip} is just a fixed multiple of the shank radius r_{Cap}:

$$f_{s/c} \equiv \frac{r_{\mathrm{Tip}}}{r_{\mathrm{Cap}}}. \tag{C.15}$$

We will define the angle β so that

$$\cos(\beta) = \frac{r_{\text{Cap}}}{r_{\text{Tip}}} = \frac{1}{f_{s/c}}. \tag{C.16}$$

Writing $z_A = z_{\text{Shank}} - z_{\text{Cap}}$ and $z_{\text{Cap}} = r_{\text{Tip}} - z_S$ and considering the central triangle to see that $z_S = r_{\text{Tip}} \sin(\beta)$ we can write

$$z_A = z_{\text{Shank}} + r_{\text{Tip}}(\sin(\beta) - 1)$$

We calculate derivatives as before. This time our expression for the derivative of z_{Shank} is

$$\frac{dz_{\text{Shank}}}{dr_{\text{Tip}}} = \frac{\cos(\beta)}{\tan(\alpha)}$$

so our expression for the full derivative is

$$\frac{dz_A}{dr_{\text{Tip}}} = \frac{\cos(\beta)}{\tan(\alpha)} + \sin(\beta) - 1.$$

Changing from terms of β to f we get

$$\frac{dr_{\text{Tip}}}{dz_A} = K_{\alpha,f} = \frac{f_{s/c}\tan(\alpha)}{1 - f_{s/c}\tan(\alpha) + \tan(\alpha)\sqrt{f_{s/c}^2 - 1}} \tag{C.17}$$

Note that the condition for tangential continuity is $f_{s/c} = \sec(\alpha)$.

Analysis Volume Calculation

In this section we calculate the size of the analysis volume incorporating a fixed shank angle and image compression. Looking at Fig. C.4, one can see that the acquired analysis volume has three geometric components:

- A spherical cap on top defined by the initial tip radius r_{Tip}^0 and the point of intersection of the sphere with the analysis cone, Z_0'
- The main analysis cone section from Z_0' to Z_1'
- A spherical cap, *not acquired*, on the bottom defined by the final tip radius r_{Tip}^1 and the point of intersection of the sphere with the analysis cone, Z_1'

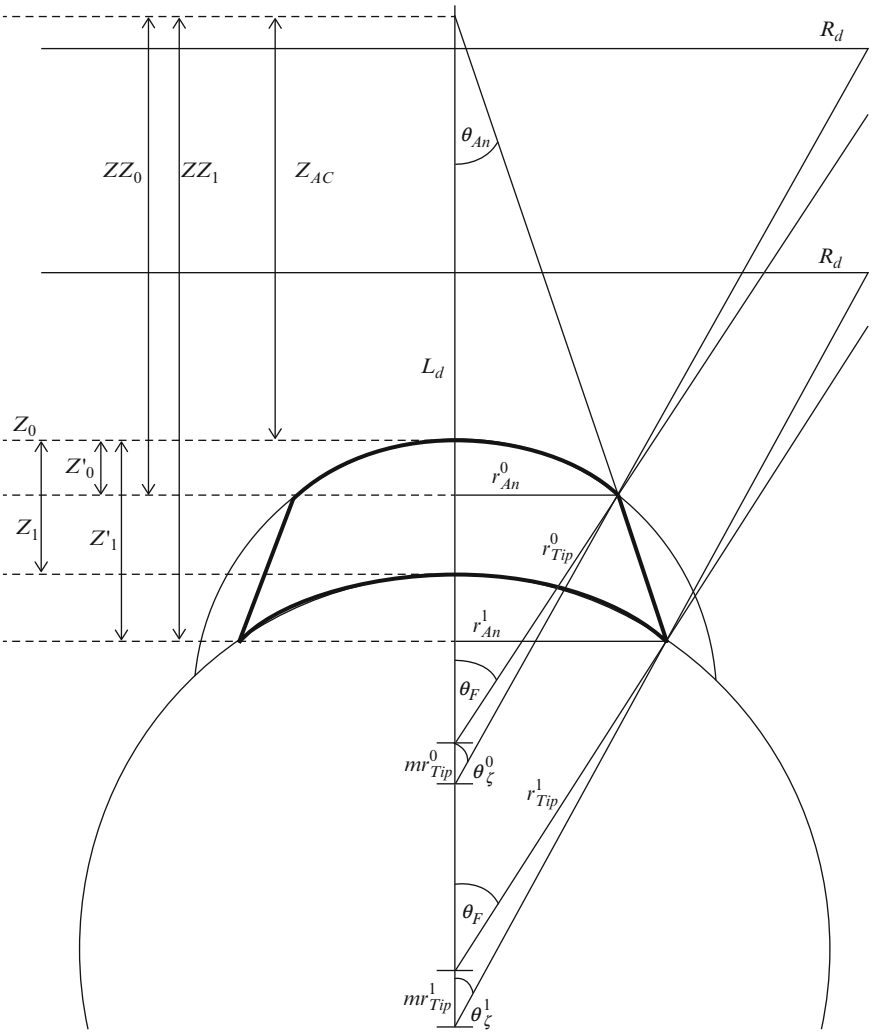

Fig. C.4 Tip geometry for analysis volume calculations

So our analysis volume equation is

$$V_{\text{Spec}} = V_{\text{Cap0}} + V_{\text{Cone}} - V_{\text{Cap1}} \tag{C.18}$$

$$V_{\text{Cap}} = \pi\left(R^2 z - \frac{z^3}{3}\right)_{z=Z}^{z=R} = \pi\left(\frac{2R^3}{3} - R^2 Z + \frac{Z^3}{3}\right).$$

For both the top and bottom cap sections, the relevant radius is the current tip radius r_{Tip}, and the Z of interest is z_{S} as defined by (C.7):

$$z_{\mathrm{S}} = r_{\mathrm{Tip}}(\gamma \cos(\theta_{\mathrm{Det}}) - m)$$

so each of the two cap sections can have their volumes written as

$$V_{\mathrm{Cap}} = \pi r_{\mathrm{Tip}}^3 \left(\frac{2}{3} - (\gamma \cos(\theta_{\mathrm{Det}}) - m) + \frac{(\gamma \cos(\theta_{\mathrm{Det}}) - m)^3}{3} \right). \tag{C.19}$$

For the purposes of presentation convenience we define the constant

$$f = \gamma \cos(\theta_{\mathrm{Det}}) - m$$

Note that this is different from the apex shape parameter $f_{S/C}$. So

$$V_{\mathrm{Cap}} = \pi r_{\mathrm{Tip}}^3 \left(\frac{2}{3} - f + \frac{f^3}{3} \right).$$

Generically, the volume of a cone section is

$$V_{\mathrm{Cone}} = \pi \tan^2(\theta) \left(\frac{z^3}{3} \right)_{z=Z_0}^{z=Z_1}$$

In our case, we need to evaluate

$$V_{\mathrm{Cone}} = \frac{\pi}{3} \tan^2(\theta_{\mathrm{An}}) \left(ZZ_1^3 - ZZ_0^3 \right).$$

It is important to note that θ_{An} is not the specimen shank angle but rather describes how the FOV evolves through the analysis depth. From Fig. C.4, we see that

$$\tan(\theta_{\mathrm{An}}) = \frac{r_{\mathrm{An}}^0}{ZZ_0}$$

where

$$ZZ_0 = Z_{\mathrm{AC}} + Z_0'.$$

Recalling (C.6)

$$r_{\mathrm{An}}^0 = \gamma r_{\mathrm{Tip}}^0 \sin(\theta_{\mathrm{Det}})$$

by definition of $K_{\alpha,f}$, we have

$$Z_{\mathrm{AC}} = \frac{r^0_{\mathrm{Tip}}}{K_{\alpha,f}}$$

Using (C.7),

$$z_0^{'} = r^0_{\mathrm{Tip}} - r^0_{\mathrm{Tip}}(\gamma \cos(\theta_{\mathrm{Det}}) - m)$$

So

$$ZZ_0 = \frac{r^0_{\mathrm{Tip}}}{K_{\alpha,f}} + r^0_{\mathrm{Tip}}(1 - \gamma \cos(\theta_{\mathrm{Det}}) + m)$$

Then

$$\tan(\theta_{\mathrm{An}}) = \frac{\gamma r^0_{\mathrm{Tip}} \sin(\theta_{\mathrm{Det}})}{\frac{r^0_{\mathrm{Tip}}}{K_{\alpha,f}} + r^0_{\mathrm{Tip}}(1 - \gamma \cos(\theta_{\mathrm{Det}}) + m)}.$$

We simplify this to

$$\tan(\theta_{\mathrm{An}}) = \frac{\gamma \sin(\theta_{\mathrm{Det}}) K_{\alpha,f}}{1 + (\xi - \gamma \cos(\theta_{\mathrm{Det}}))K_{\alpha,f}}.$$

For the purposes of presentation convenience we define the constants

$$g = \gamma \sin(\theta_{\mathrm{Det}})$$
$$\kappa = 1 + (\xi - \gamma \cos(\theta_{\mathrm{Det}}))K_{\alpha,f}$$

With this notation change

$$\tan(\theta_{\mathrm{An}}) = \frac{gK_{\alpha,f}}{\kappa}$$

$$ZZ_0 = \frac{\kappa r^0_{\mathrm{Tip}}}{K_{\alpha,f}}$$

$$ZZ_1 = \frac{\kappa r^1_{\mathrm{Tip}}}{K_{\alpha,f}}$$

So our final V_{Cone} is

$$V_{\text{Cone}} = \frac{\pi}{3}\left(\frac{gK_{\alpha,f}}{\kappa}\right)^2\left(\frac{\kappa}{K_{\alpha,f}}\right)^3\left(\left(r_{\text{Tip}}^1\right)^3 - \left(r_{\text{Tip}}^0\right)^3\right)$$

$$V_{\text{Cone}} = \frac{\pi g^2\kappa}{3K_{\alpha,f}}\left(\left(r_{\text{Tip}}^1\right)^3 - \left(r_{\text{Tip}}^0\right)^3\right).$$

Putting the volume terms all together we find

$$V_{\text{Spec}} = \frac{\pi g^2\kappa}{3K_{\alpha,f}}\left(\left(r_{\text{Tip}}^1\right)^3 - \left(r_{\text{Tip}}^0\right)^3\right) + \pi\left(\frac{2}{3} - f + \frac{f^3}{3}\right)\left(\left(r_{\text{Tip}}^0\right)^3 - \left(r_{\text{Tip}}^1\right)^3\right)$$

Simplifying

$$V_{\text{Spec}} = \frac{\pi}{3}\left\{\frac{g^2\kappa}{K_{\alpha,f}} + \left(3f - 2 - f^3\right)\right\}\left(\left(r_{\text{Tip}}^1\right)^3 - \left(r_{\text{Tip}}^0\right)^3\right). \tag{C.20}$$

Volume Increment

During reconstruction, we process a sequence of atoms that have various assigned volumes. After reconstructing atom i with assigned volume Ω_i, we need to adjust the height of the model specimen as if this volume had been removed uniformly from the spherical surface of the FOV. Accounting for an expected detector efficiency ε, the z adjustment we make is

$$\Delta z_{\text{Tip}} = \left(\frac{\mathrm{d}z_{\text{Tip}}}{\mathrm{d}V_{\text{Spec}}}\right)\frac{\Omega_i}{\varepsilon}.$$

So we need to take the derivative of volume expression (C.20). This is pretty straightforward since for our standard reconstruction all of the terms are constants except r_{Tip}:

$$\frac{\mathrm{d}r_{\text{Tip}}}{\mathrm{d}z_{\text{Tip}}} = K_{\alpha,f}.$$

So the reconstruction volume change per unit volume is

$$\frac{\mathrm{d}V_{\text{Spec}}}{\mathrm{d}z_{\text{Tip}}} = \pi\left\{g^2\kappa + K_{\alpha,f}\left(3f - 2 - f^3\right)\right\}r_{\text{Tip}}^2$$

and our volume increment becomes

$$\Delta z_{\mathrm{Tip}} = \frac{\Omega_i}{\varepsilon\pi\left\{g^2\kappa + K_{\alpha,f}\left(3f - 2 - f^3\right)\right\}r_{\mathrm{Tip}}^2}.$$

If we assume that the shank angle is zero, then $K_{\alpha,f}$ is zero. In the limit of small-angle we obtain a per-atom z increment of

$$\Delta z_{\mathrm{Tip}} = \frac{\Omega_i L_{\mathrm{Det}}^2}{r_{\mathrm{Tip}}^2 \varepsilon\pi R_{\mathrm{Det}}^2 \xi^2}.$$

Determining Specimen Shank Angle from the Voltage History Plot

Starting with our formula for the acquisition volume (C.20) we note that all shank angle dependence is in the $K_{\alpha,f}$ terms, so we consolidate the remaining terms into a placeholder, λ, and write

$$V_{\mathrm{Spec}} = \frac{\pi}{3}\left\{\frac{g^2}{K_{\alpha,f}} + \lambda\right\}\left(\left(r_{\mathrm{Tip}}^1\right)^3 - \left(r_{\mathrm{Tip}}^0\right)^3\right)$$

where

$$\lambda = g^2(\xi - \gamma\cos(\theta_{\mathrm{Det}})) + \left(3f - 2 - f^3\right).$$

Solving for $K_{\alpha,f}$ we find

$$K_{\alpha,f} = \frac{\pi g^2 S_{\mathrm{VR}}}{3 - \lambda\pi S_{\mathrm{VR}}} \tag{C.21}$$

where

$$S_{\mathrm{VR}} = \frac{\left(r_{\mathrm{Tip}}^1\right)^3 - \left(r_{\mathrm{Tip}}^0\right)^3}{V}.$$

The volume V_{Spec} is typically accumulated from the assigned atomic volumes, and the initial and final tip radii are evaluated with $R = v/KF$. So we will typically use

$$S_{\mathrm{VR}} = \frac{\varepsilon\left(\left(v_{\mathrm{Tip}}^1\right)^3 - \left(v_{\mathrm{Tip}}^0\right)^3\right)}{(FK)^3\sum\Omega}$$

Substituting (C.17) into (C.21) and gathering terms of tan (α) we find

$$\tan(\alpha) = \frac{\pi g^2 S_{VR}}{f_{S/C}(3 - \lambda\pi S_{VR} + \pi g^2 S_{VR}) - \pi g^2 S_{VR}\sqrt{f_{S/C}^2 - 1}} \tag{C.22}$$

In the case of tangential continuity, α satisfies

$$\sin(\alpha) = \frac{\pi g^2 S_{VR}}{3 - \lambda\pi S_{VR} + \pi g^2 S_{VR}}. \tag{C.23}$$

References

1. Blavette, D., Sarrau, J.M., Bostel, A., Gallot, J.: Direction et distance d'analyse a la sonde atomique. Rev. Phys. Appl. **17**, 435–440 (1982)
2. Bas, P., Bostel, A., Deconihout, B., Blavette, D.: A general protocol for the reconstruction of 3D atom probe data. Appl. Surf. Sci. **87/88**, 298–304 (1995)
3. Walck, S.D., Buyuklimanli, T., Hren, J.J.: Extended depth profiling with the IAP. J. Phys. **47-C2**(3), 451–458 (1986)
4. Miller, M.K.: Atom Probe Tomography: Analysis at the Atomic Level. Kluwer Academic/Plenum Publishers (2000)

Appendix D: Mass Spectral Performance

Analytical Basis for TOF Spectrometry

As a time of flight (TOF) mass spectrometer, the mass resolving power (MRP) of an atom probe is one of the critical parameters that describe its performance. On the surface, this parameter seems straightforward to define and measure. However, as we shall see below, there are many subtleties that can influence the determination and reporting of MRP [1].

Determining the Timing and Energy Components of Time of Flight

A first-order analysis is commonly used to derive the functional dependence of timing uncertainties in APT. If the potential energy gain of an ion (neV) is equated to the final kinetic energy ($mv^2/2$) and the limit is considered where potential energy is immediately converted to kinetic energy so that ion speed can be considered as constant over the flight path ($v = L/t$), then

$$nev = \frac{1}{2}mv^2 = \frac{1}{2}m\frac{L^2}{t^2} \tag{D.1}$$

where n is the charge state, e is the elementary unit of charge, V is the potential difference, m is the ion mass, v is the ion speed, L is the ion flight path length, and t is the ion TOF; then the resulting equation may be solved for TOF as

$$t^2 = \frac{m}{n}\frac{L^2}{2ev}. \tag{D.2}$$

D.J. Larson et al., *Local Electrode Atom Probe Tomography: A User's Guide*,
DOI 10.1007/978-1-4614-8721-0, © Springer Science+Business Media New York 2013

For a given ion type, m, n, and e are constants and differentiating (D.2) gives

$$\Delta t = \frac{t}{2}\left(2\frac{\Delta L}{L} - \frac{\Delta V}{V}\right). \tag{D.3}$$

If a single ion type is measured multiple times with a perfect timer, then the timing variation that develops is due to voltage ($\Delta V/V$) or flight length ($\Delta L/L$) variations. This component of timing precision will be referred to as the physical timing uncertainty, δt_P:

$$\delta t_P = \Delta t = t\left(\frac{\Delta L}{L} - \frac{1}{2}\frac{\Delta V}{V}\right). \tag{D.4}$$

Timer electronics achieve a finite precision which will be denoted as δt_T. This imprecision is independent of the physical timing imprecision. Furthermore, there is timing uncertainty associated with the temporal duration of field evaporation during a pulse. This term is called time-of-departure spread (TODS) and is denoted as δt_D. This timing imprecision is also independent of both the timer precision and the physical timing precision. These three terms may be added in quadrature as follows:

$$\delta t^2 = \delta t_P{}^2 + \delta t_T{}^2 + \delta t_D{}^2. \tag{D.5}$$

Putting this all together yields

$$\delta t^2 = t^2\left(\frac{\Delta L}{L} - \frac{1}{2}\frac{\Delta V}{V}\right)^2 + \delta t_T{}^2 + \delta t_D{}^2. \tag{D.6}$$

Finally, MRP is related to the time resolving power through (D.2) by noting that

$$2\left(\frac{\delta t}{t}\right) = \frac{\delta m}{n}\Big/\frac{m}{n} \tag{D.7}$$

or

$$\mathrm{MRP} \equiv \frac{m}{\delta m} = \frac{1}{2}\frac{t}{\delta t} = \frac{1}{2\delta t}\sqrt{\frac{m}{n}\frac{1}{2eV}}L. \tag{D.8}$$

From (D.2) it is apparent that flight time, and hence MRP, will vary with $\sqrt{\frac{m}{n}}$, $\sqrt{V^{-1}}$, and L. Thus if MRP is to be compared from one experiment to the next, it must be reported at standard values for m/n, V, and L, or the values must be stated explicitly.

Sources of ΔV/V

Normalized energy deficits, $\Delta E/E$, which can come from a variety of sources, are indistinguishable from voltage fluctuations in the accelerating voltage, $\Delta V/V$, and so all such terms will be grouped in the $\Delta V/V$ term. When doing this, it is essential to remember that a ΔV operating on an ion of $n = +2$ produces a ΔE that is twice that of an $n = +1$ ion. When a large energy spread exists, flight time differences for a given ion type get worse with longer total flight time, and longer flight paths do not lead to improved timing resolution. In laser pulsing, energy deficits may be small if they are primarily due to thermal energy spreads (0.025 eV at 300 K). Thus the TOF spread, δt, is unchanged during ion flight, and greater MRP can be achieved by making the flight time longer. This effect was demonstrated dramatically by Liu et al. [2] where they achieved MRP of 4,000 by making very long flight times in an 8-m-long laser pulsed atom probe.

In voltage pulsing, energy spreads develop because the accelerating voltage is pulsed by $\Delta V/V \approx 20$ % to induce synchronized field evaporation events. The field evaporation event actually occurs over a narrower range of voltage which induces energy spreads of $\Delta E/E = \Delta V/V \approx 1$–$2$ % for $n = +1$ ions. This is a large value which limits MRP in voltage pulsing to about 200 regardless of flight path length unless some additional measure is taken (e.g., local electrode or reflectron) to counter this effect. In LEAPs, the energy spread in field pulsing is reduced compared to a remote electrode geometry because the distance over which any ion is accelerated is reduced (distance between tip and aperture of local electrode) and the ion enters the field-free region of the flight path more quickly.

Sources of ΔL/L

The flight length of an ion, L, is generally stated for the distance to the center of the detector (or the shortest distance to the detector in the case of a reflectron-based system). In APT, the detector records hit position coordinates on the detector which makes it possible to correct for geometric differences in flight length with angle from the central axis such that all flight times are corrected to correspond to L. In the LEAP, a flight length correction known as the bowl correction was developed by Oltman [3] and is discussed in detail in Chap. 4.

Sources of $\delta t_T/t$

The imprecision of the clocks used to time ion flights is a hard limit on the timing precision. However, there are other factors that may limit precision further. The imprecision introduced by the electronics that pick an arrival time from pulses that

have traversed the delay line anode (DLA) is likely to be greater than the clock imprecision and is usually the largest limitation imposed by the hardware. Furthermore, this limitation can vary across the face of any DLA. MCPs generally have a fast response and low time spread relative to the timer precision, so they should not degrade the precision overall.

Sources of $\delta t_D/t$

Physically, the temporal spread of the evaporation window is the sum in quadrature of the timing imprecisions. In field pulsing, voltage pulses of a few nanoseconds are used, but the evaporation events are restricted to the topmost portion of the pulse and the TODS is correspondingly small for good electrical conductors. The energy spread terms dominate in field pulsing.

For thermal pulsing, energy variations can be small, and it is the TODS that usually dominates. The challenge for making small TODS is cooling the specimen quickly after heating. Certainly, heating the smallest possible volume helps accomplish this. It is for this crucial reason that laser-capable LEAPs have always been designed to focus to the smallest possible spot size. The shortest TODS reported to date was 114 ps on an aluminum specimen (good thermal diffusivity) with 355 nm laser light on a LEAP 4000X ($<$3 μm diameter, 4σ spot) [1]. Note that this TODS is much greater than the 12 ps pulse width of the laser which is a confirmation that the cooling time dominates the TODS. Other materials, such as steels, can have more shallow skin depths (depth over which energy is absorbed) than aluminum which can also aid in heating small volumes and result in a reduction in TODS.

Discrete vs. Collective Discrimination

In assessing the impact of MRP on a set of measurements, it is important to distinguish between whether the goal is image quality or composition determination. For image quality, the goal is high confidence in the identity of each atom shown in the image. Ideally, this requires full discrimination and very high MRP for all peaks in the mass spectrum. For composition determination, the goal is to correctly determine the number of atoms of each type in some volume of material. Methods are available to decouple overlapping features in a mass spectrum to obtain accurate bulk compositions. Thus a distinction is made here between discrete and collective discrimination.

Discrete discrimination is defined as the ability to discern the identity of each individual ion in a dataset. In APT, discrete discrimination is required for imaging so that each ion in the dataset may be correctly assigned an identity. An example of the importance of discrete discrimination is shown in Fig. D.1. Here the very low oxygen signal (obtained from a peak at $m/n = 16$ Da) is obscured by the tail of

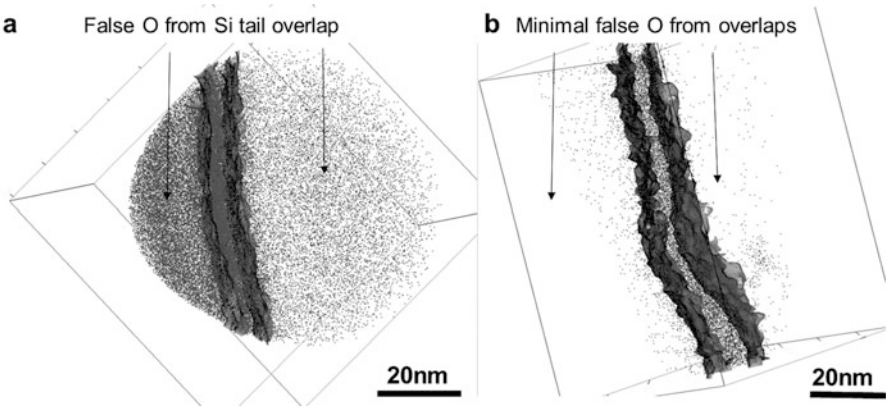

Fig. D.1 The role that discrete discrimination plays in image quality in APT. In (**a**) the apparent oxygen signal in the silicon substrate (*right side* of image) is due to overlap with the large tail from the silicon peaks. In (**b**) with greater MRP comes improved discrete discrimination, so there is no misidentified oxygen signal in the silicon substrate to the *right*. Although the peaks may be decomposed collectively to obtain accurate bulk composition, (**b**) shows the benefit of discrete discrimination for imaging as very few oxygen atoms are actually present in the substrate silicon

strong silicon signals (located at $m/n = 14$, 14.5, and 15 Da) in the mass spectrum. Even though a clear oxygen peak is observed at 16 Da, a majority of the counts in this mass range are actually silicon ions. Since there is no way to discriminate individual ions that have different identities but the same m/n, these signals cannot be discriminated discretely in an image.

Collective discrimination is defined as the ability to discern, as a fraction of some group, the identity of each subgroup. Collective discrimination would be accomplished, for example, by decomposition of a single unresolved peak or overlapping peaks into their constituents using deconvolution or isotopic distribution information (see Chap. 6). Collective discrimination is important for determination of bulk composition within a particular volume.

In Fig. D.2, this distinction is illustrated with regard to resolving two peaks. For collective discrimination, it should be possible to separate two peaks by deconvolution when there are enough counts to perform a statistically significant separation. For peaks of about equal height, as shown in Fig. D.2a, discrimination is possible when they are separated by their FWHM.

For discrete discrimination, the requirements on MRP are much greater. Ideally, every atom displayed would be unambiguously identified. For discussion purposes, the minimum requirement is five times that for collective discrimination ($5 \times$ FWHM), as shown in Fig. D.2b. When peaks are not of equal magnitude or width, or when the number of counts is low, then these peak separations may need to be even greater.

A practical example is shown in Fig. D.3. Here the $^{28}Si^{+}$ peak and the $^{14}N_2{}^{+}$ peak are just separated enough for good collective discrimination. A composition determined from this volume would be expected to have good accuracy; however, if

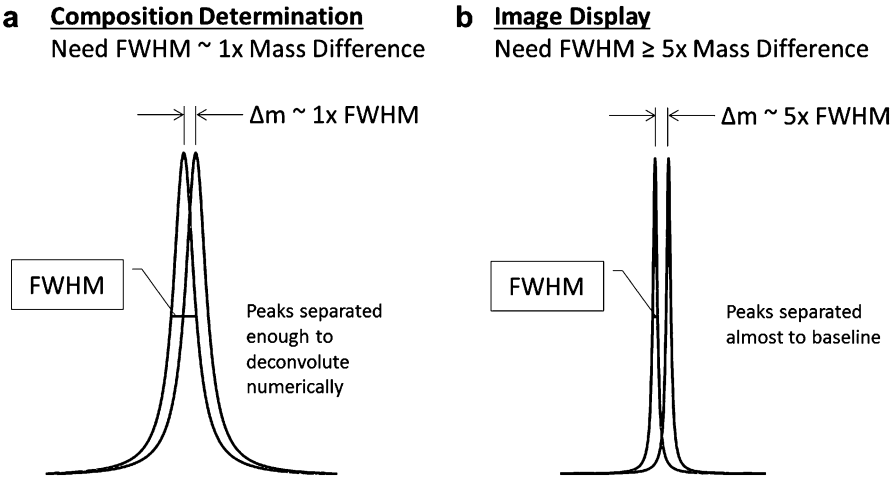

Fig. D.2 Examples of peak overlaps for peaks of equal magnitude. The MRP in (**a**) is adequate for collective peak discrimination through deconvolution. The peaks in (**b**) are much more separated, relative to their width making discrete discrimination possible

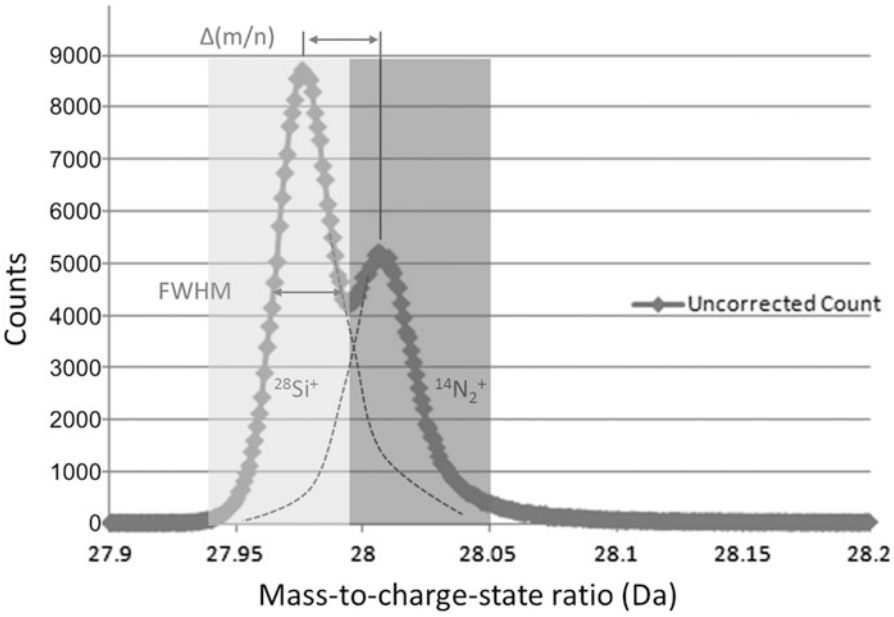

Fig. D.3 Collective discrimination of the $^{14}N_2^+$ and $^{28}Si^+$ peaks. With sufficient counts, numerical decomposition is straightforward. The *two shaded boxes* are placed such that they meet at the minimum between the peaks to suggest the usual range delimiters that might be used in plotting these counts in an image

ranges were set as shown by the two shaded areas, then many of the counts in each range would be misidentified. Discrete display of the hits in this spectrum using these ranges would lead to a more ambiguous result. The conclusion of this discussion is that the required MRP depends strongly on whether composition determination or image display is the analytical goal.

Standard MRP

MRP values can be experimentally measured for a wide range of operating conditions. As shown in (*D.8*), MRP depends on m/n, L, and V. However, there are situations where a single standard value of MRP is useful. For example, comparison of general instrument performance demands a metric that enables comparison of mass spectrum quality. In order to compare MRP from one measurement to another, one must either make measurements at the same m/n, L, and V or refer measurements to the same m/n, L, and V.

For these reasons, MRP at a standard operating condition on a standard specimen is highly desirable. Aluminum is a convenient material on which to make MRP measurements because it is easy to prepare in wire form (which makes it universally applicable to all atom probes), it has a single isotope, and it has a very high thermal diffusivity (it can produce high MRP in both laser and voltage pulsing modes). Therefore, we propose that when making claims about instrument performance, a standard MRP is reported based on the $^{27}Al^{+}$ peak. Ideally, the operating voltage, field of view, crystallographic orientation, and other factors should be standardized as well.

References

1. Oltman, E., Kelly, T.F., Prosa, T.J., Lawrence, D., Larson, D.J.: Measuring contributions to mass resolving power in atom probe tomography. Microsc. Microanal. **17**(S2), 754–755 (2011)
2. Liu, J., Wu, C.-w., Tsong, T.T.: Measurement of the atomic site specific binding energy of surface atoms of metals and alloys. Surf. Sci. **246**(1–3), 157–162 (1991)
3. Oberdorfer, C., Eich, S.M., Schmitz, G.: A full-scale simulation approach for atom probe tomography. Ultramicroscopy **128**, 55–67 (2013), doi: http://dx.doi.org/10.1016/j.ultramic.2013.01.005

Appendix E: Additional Considerations for LEAP Operation

Before routine work on a LEAP can be pursued, there are certain instrument calibrations and preparations that must be made. This appendix summarizes the essential considerations that should be made before routine operation of the LEAP.

Calibration Files

The conversion of 2D time-of-flight (TOF) data into a mass spectrum is instrument dependent and, to a lesser extent, specimen dependent. The first data collected from a calibration specimen is used to determine characteristic voltage and bowl corrections (see Chap. 5) used for subsequent analyses. In order to optimize each mass spectrum, a unique voltage and bowl correction must be done for each LEAP analysis; however, the characteristic corrections from the calibration analysis serve to enable accurate conversion from TOF to mass-to-charge ratio (m/n) and enables live display of the mass spectrum during data collection. For details on how to create a calibration file, see the LEAP User Manual.

A properly calibrated LEAP likely has multiple calibration files available for selection. Choosing the one that best matches the experimental geometry ensures that a high-quality live mass spectrum is generated. For example, upon initial installation, a LEAP might have four calibration files: silicon microtip voltage pulse and laser pulse analyses as well as aluminum wire voltage pulse and laser pulse analyses. Ideally, each analysis was from a specimen with data acquired over a large range of acquisition voltages to ensure a stable calibration over a wide variety of experimental conditions. The characteristic calibration performs best when a specimen of similar geometry (microtip or wire) and acquisition voltage is used. Failure to use an appropriate calibration file may cause the live mass spectrum to have broader mass peaks that drift in m/n position as the acquisition

D.J. Larson et al., *Local Electrode Atom Probe Tomography: A User's Guide*,
DOI 10.1007/978-1-4614-8721-0, © Springer Science+Business Media New York 2013

voltage changes. Fortunately, this only impacts the live mass spectrum quality. Each individual analysis is properly corrected as a step in data processing (Chap. 5), so the quality of the reconstructed data will not be impaired by a choice of a calibration file that does not match the experimental conditions well.

The Local Electrode

Local electrodes (LEs) are critical for good LEAP performance (for a detailed description of the LE see Chap. 3). Each LE is factory tested to ensure good ultrahigh-vacuum (UHV) compatibility, correct shape, and high resistance to electron emission through the voltage operation range of the LEAP. The nature of APT is to analyze specimens that fail with some significant probability. With each failure there is opportunity to damage the LE leading to deceased performance (i.e., partial occlusion of the open aperture itself or electron emission from the LE that results in a very poor signal-to-noise ratio). A challenge of tool management is to store, test, and clean LEs in a way that ensures maximum performance and lifetime. New electrodes from CAMECA have been qualified for electrical performance to 15 kV with less than 0.2 % data rate (DR) using the procedure outlined in the Local Electrode Flat-Test Procedure technical bulletin.

Storage

LEs are designed to operate in both voltage pulsed and laser pulsed modes. The plastic insulator (polyether ether ketone or PEEK) that separates the voltage pulsed nickel apex from the grounded puck body absorbs moisture when exposed to a non-UHV environment. Consequently, LEs should be stored in the LEAP when possible and for best results should reside in the instrument for 3–7 days before being used to analyze specimens. A dust-free, dry-pumped vacuum storage unit is the best alternative to the LEAP, followed by a dust-free desiccator.

Heating

It is well known that removal of adsorbed material is enhanced by heating that material while under vacuum (commonly referred to as baking) [1, 2]. LEs stored in the laboratory can be conditioned to the UHV environment of the LEAP more rapidly when properly baked. An optional LEAP upgrade is the load-lock heater which is designed to significantly reduce the conditioning period. Those without a load-lock heater can consider baking in a vacuum oven and placing a hot carousel of LE pucks immediately into the LEAP to gain some reduction in the

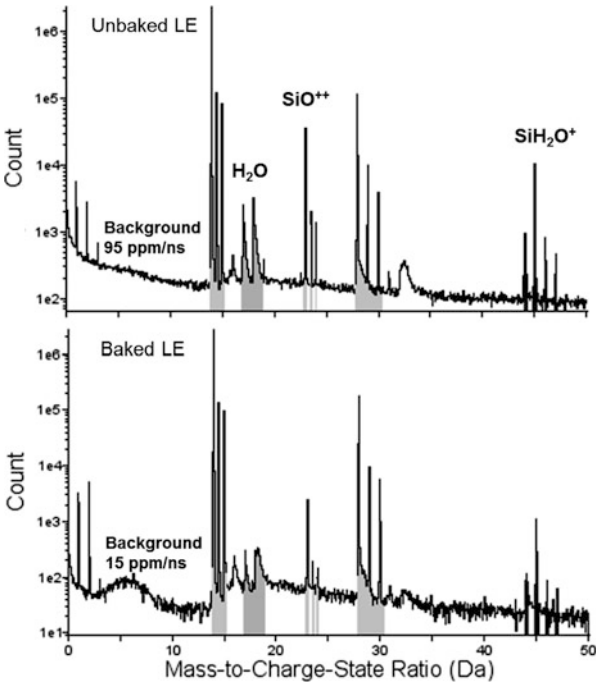

Fig. E.1 Typical improvement in mass spectra for water-based ion contamination originating from LEs after 4 h under vacuum. Spectra from an LE with no load-lock heating (*top*) are compared to an LE which has been baked for 4 h at 150 °C (*bottom*). Note the *Y*-axis scale offset

conditioning period. Figure E.1 shows the mass spectra from a silicon microtip analyzed with an LE that has been put into service 4 h after storage outside of vacuum (unbaked) and another LE that has been baked for 4 h and put into service. The microtip is made of antimony-doped silicon and, after analyzing through the surface, should not contain oxygen or hydrogen. The relative number of detected events associated with contamination (peaks labeled H_2O, SiO, and SiH_2O) is reduced from 3.5 to 0.35 % of the total spectrum for the baked LEs.

Generally, electrodes stored in the LEAP do not experience changes in electrical performance unless put into service. For example, an LE that tests to 10 kV (shows electron emission) will continue to test to 10 kV even after a month of storage within the LEAP buffer chamber. Though time in UHV does not affect electrical performance it does impact the presence of water-bearing and hydrogen-bearing contamination emitted during acquisition. For any unbaked LEs that experience contact with the ambient environment, it is recommended that they be placed in LEAP UHV for a minimum of 3–7 days before being put into service. Long-term trends for a group of baked and unbaked LEs are shown in Fig. E.2. A bake of local electrodes in the load lock for 4 h at 150 °C appears equivalent to conditioning LEs under vacuum without baking for 4 days (note that the unbaked LE results are shifted by 96 h to highlight the trend). The additional downward curvature of the baked LE contamination trends immediately after baking for the H_2O and SiO peaks suggests that time in vacuum alone may not be sufficient to achieve the best cleanliness for LEs.

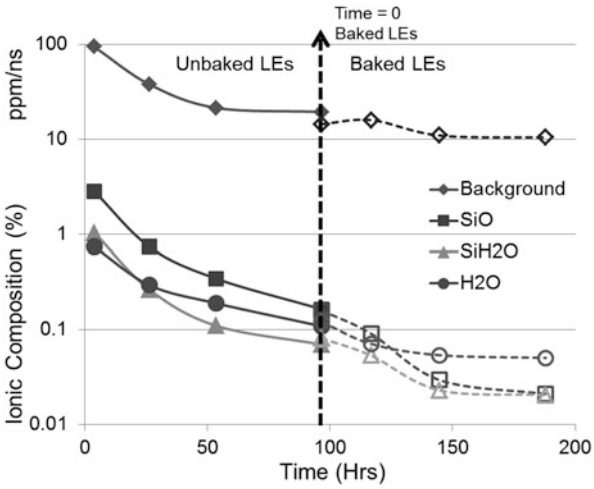

Fig. E.2 Typical improvement in total water-based ion contamination for baked and unbaked LEs over a 4-day period in vacuum

Testing

Electron emission from the local electrode, referred to as electrode turn-on, is the primary failure mode that limits LE lifetime. Sharp debris or damage to the LE surface produces a geometry that enables Fowler–Nordheim electron emission [3]. It is believed that this emission current terminates somewhere on the specimen, enabling ion emission that at some critical voltage overwhelms the normal imaging operation of the atom probe (see Fig. E.3). Depending on the type of debris or damage, either these emission regions on the LE can be mitigated through plasma treatments or they may require refurbishment of the LE assembly with a new aperture cone.

Testing for electron emission is illustrated in Fig. E.4. The LE is positioned over a flat test sample (aligned in this case near a microtip for reference) in distance similar to normal microtip analysis (~150 μm above the test flat). This distance is based on the measured separation between the LE and its reflection (see the CAMECA Local Electrode Flat-Test Procedure technical bulletin for instrument-specific details). LEs are considered safe to use with a specimen up to the voltage for which the flat-test begins to exhibit significant emission (0.2 % DR or measured electron current). Minimum electrical turn-on performance guidelines suggest that the maximum operational voltage for analysis of a wire specimen is 1.5–2.0 times the flat-test value and for a microtip specimen is 1.2–1.4 times the flat-test value due to the higher electric field imposed upon the electrode surface when running microtips due to the microtip geometry.

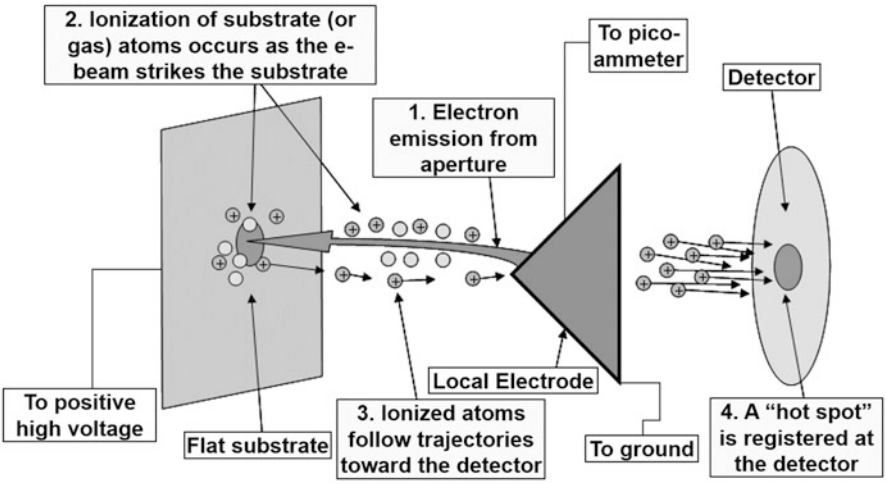

Fig. E.3 Schematic illustrating possible sources of observed LE electron emission. (*1*) Fowler–Nordheim electron emission from LE. (*2*) Ionization of gas and/or substrate atoms when electron beam travels to high-voltage surface and strikes substrate surface. (*3*) Ionized material follows electric field to terminate on LE or passes through to the detector. (*4*) High-ion-emission region (hot spot) observed at detector (as well as broader emission region) indicating significant LE emission

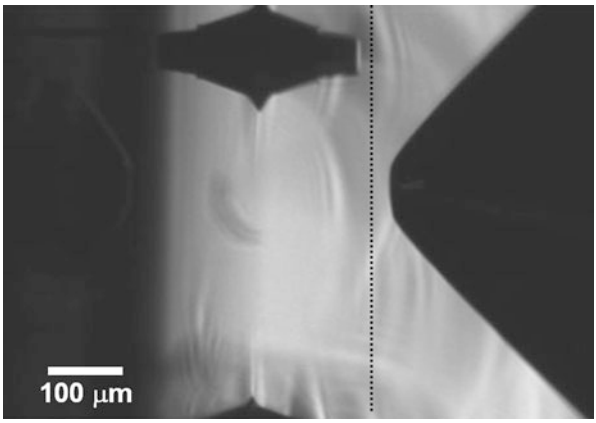

Fig. E.4 SEM image of LE alignment used for the electron emission flat-test. The separation between LE-reflected image (*left*) and the direct image (*right*) is used to estimate the distance between flat substrate and the LE

Plasma Treatment

Plasma treatment has been found to improve the electron emission characteristics of LEs in general. The precise nanoscale modifications to the LE are not well understood, but the benefits are clear. During the LE plasma treatment process, the plasma likely removes carbonaceous contamination leading to a cleaner surface. For recovering damaged or contaminated LEs, plasma treatment can improve flat-test turn-on voltages by 5–10 kV in some cases.

Best Known Practices

Once electrodes leave vacuum storage at the factory, they are prone to pick up small particle contamination of various sorts. Should these particles be of the right size, shape, and location, they can degrade the electrical performance of the electrode. This degradation in flat-test performance can almost always be undone (~95 % of cases) with proper conditioning of the electrode. In order to remove problematic contamination, the following procedures should be followed for new electrodes introduced from an ambient environment into the UHV environment of the LEAP:

1. Immediately before entry into the load lock, electrodes should be physically treated with a flow of clean, dry, ~15 psig pressure gas (canned dry air or N_2) to remove any loose particle contamination on the electrode surface. Spray gas directly at the front opening of the electrode (position a few centimeters away and spray for 1–2 second bursts).
2. If available, then plasma treat the electrode for 12 h with the integrated plasma treatment system (check with CAMECA for guidelines regarding gas type, power, and pressure of operation for the plasma).
3. Perform a flat-test procedure as described in the technical bulletin by turning up voltage until a DR of 0.2 % is achieved or upon reaching 11 kV. Sometimes an electrical discharge may occur, requiring the operator to perform the test again. These electrical discharges often remove stubborn particle contamination that has not been removed via the high-pressure gas and plasma treatments and should not necessarily be avoided for new electrodes. These electrical discharges often happen after introduction of new electrodes into the LEAP from storage in air and do not negatively affect the performance of new electrodes.
4. Should electrodes fail to yield satisfactory flat-test results, then repeat the gas flow and plasma treatment an additional time. If plasma treatment is unavailable, then remove and repeat physical treatment with gas and re-test.
5. Any new electrode failing to meet minimal electrical performance characteristics upon entry and after testing/conditioning described above should be immediately returned for replacement/requalification (contact your CAMECA service representative for details).
6. For the purposes of acquiring the highest quality data possible, electrodes should be placed into the LEAP as soon as received from CAMECA and tested/conditioned for subsequent use. Should space considerations require that some electrodes need to be stored external to the LEAP, keep them covered and in a dry, oil-free, dust-free environment and test/condition them upon entry into the LEAP.

Acquisition Control

Modern atom probes utilize some form of automated acquisition algorithm to control data collection [4]. Ideally, automated control would adjust conditions to optimize analysis yield, data quality, and acquisition time; however, current algorithms merely utilize some form of voltage manipulation in order to maintain a desired DR. Alternative control strategies continue to be developed. See your control software user manual for the latest implementation.

Main Voltage Control Algorithm

LEAP automated acquisition control dictates voltage steps by way of a proportional control algorithm defined in the EvapControl.INI file using six parameters. Opening or editing INI files should only be done after consultation with CAMECA to avoid potentially serious problems. The general control behavior is illustrated in Fig. E.5. Here the target DR is established, and the voltage increases or decreases dependent on the average rate measured during some previous acquisition time window. As shown in the figure, when the target DR is changed from 3 to 14 %, the voltage quickly increases to raise the actual rate. Note that the actual rate is not immediately achieved. The rate at which the set point is achieved and the propensity to overshoot or undershoot the target are standard issues for control algorithms [5].

The parameterization of the LEAP control algorithm allows the user to optimize the efficiency for reaching and maintaining the DR set point by modifying the algorithm parameters. Default Algorithm 1 from LCC 4.2 is illustrated as an example below followed by a description of each of the fields following:

[Algorithm 1]
Algorithm Name = Standard
Evaporation rate moving average filter depth (pulses) = 10000
Pulses Per Voltage Update = 5000
Proportional Coefficient (%/%) = -10.0
Max upward voltage step (V) = 0.5
Max downward voltage step (V) = 0.5

- *Algorithm Name* is the name of the algorithm, up to 100 characters long. This name appears in the LEAP Control Center (LCC) Advanced Acquisition Setup window, Evaporation Control Algorithms pane, which adds the item to the pick list. If the name is set to *UNUSED*, the algorithm is disabled and does not appear in the pick list.
- *Evaporation rate moving average filter depth* (*pulses*) is the number of pulses over which the current evaporation rate is calculated. The resultant moving averaged evaporation rate is then input to the algorithm to determine the size of the next specimen-voltage change.

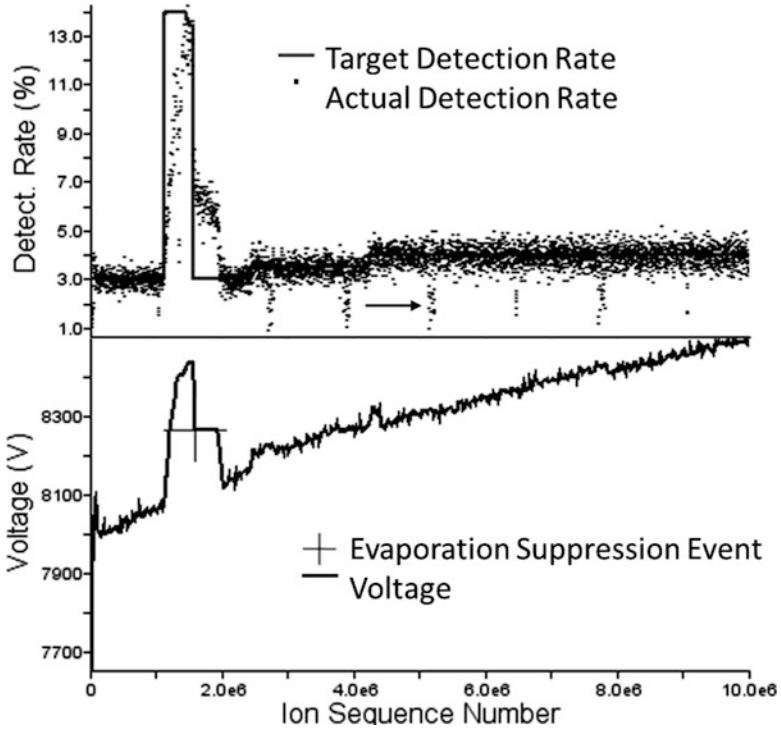

Fig. E.5 The proportional control algorithm in action showing (*top*) target and actual detection rate and (*bottom*) voltage response for the same 10 million detected events. The *arrow* shows excursions in the detected rate that occur during a typical laser Drift Comp scan. The large "+" shows the occurrence of an IEC event and the resulting fast drop in voltage which resulted in an equally fast reduction in observed detection rate

- *Pulses Per Voltage Update* specifies that after every *n* pulses the firmware calculates the current DR (based on the filter depth as determined above), calculates an error term based on the difference between the current and target DRs, and calculates a voltage-update step size equal to the product of the error term and the proportional coefficient setting. This parameter defines *n* and hence determines the frequency of voltage adjustments.
- *Proportional Coefficient* (%/%) is a multiplier for converting the detection-rate error term to a voltage adjustment value.
- *Max upward voltage step* (*V*) is the maximum upward-step size per voltage-update interval. The final voltage step for an increasing voltage step is clipped against this setting.
- *Max downward voltage step* (*V*) is the maximum downward-step size per voltage-update interval. The final voltage step for a decreasing voltage step is clipped against this setting.

- Proportional Control Algorithm Detail—The voltage step is governed by the following formula which is limited by maximum positive and negative voltage steps (examples based on Algorithm 1 for $f = 200$ kHz are illustrated following the general formula):

$$V_{\text{Step}} = \left[-V_{\text{Max Down}}, V \times \frac{\text{Prop.Coeff}}{100} \times \left(\text{DR}_{\text{Current}\%} - \text{DR}_{\text{Target}\%}\right), V_{\text{Max Up}}\right]$$
$$\xrightarrow{f=200\,\text{kHz}} \left[-0.5, -V \times 0.1\left(\text{DR}_{\text{Current}} - \text{DR}_{\text{Target}}\right), +0.5\right] \text{Volts per} \frac{1}{40}\text{s}$$

Maximum voltage slew:

$$V_{\text{Up}}(\text{Volts/s}) = f \times V_{\text{Max Up}}/N_{\text{Pulses Per Update}} \xrightarrow{f=200\,\text{kHz}} 20\,\text{Volts/s}$$

$$V_{\text{Down}}(\text{Volts/s}) = f \times V_{\text{Max Down}}/N_{\text{Pulses Per Update}} \xrightarrow{f=200\,\text{kHz}} 20\,\text{Volts/s}$$

Advanced users can edit and modify the EvapControl.INI file to include additional algorithms or modify the default algorithms. In order to reset the EvapControl.INI file to its default settings, delete or rename the EvapControl.INI file and then close and reopen the LEAP Control Center software, and a new default file is generated.

The behavior of each default algorithm is summarized in Table E.1 where the number of pulses per update is also converted to time per update for a 200 kHz pulse frequency. Typical rate determinations are averaged over a 10,000 or 50,000 pulse window. Voltages are updated every 5,000, 10,000, or 25,000 pulses depending on the specific algorithm. The proportional coefficient ranges from 0.05 to 10, while the maximum voltage change per step is between 0.5 and 5 V going upward or 0.5 and 1,000 V going downward.

When operating the LEAP, the user selects target DR and initial voltage (or engages the algorithm during the experiment), and the algorithm manipulates the voltage from there. Two of the most obvious effects of the algorithm choice are the minimum DR allowed by the software and the maximum rate of voltage increase (which will often affect the time it takes to go from near-zero ion emission to the target DR). For many materials that require low DRs to survive, only the Low Detection Rate and Interface Low Rate algorithms are appropriate, although these algorithms have reasonably large maximum upward voltage steps.

In terms of optimizing analysis yield or data quality, the current algorithms are blind. They merely try to hold the evaporation process relatively constant. Multiphase materials or layered structures can present widely varying local evaporation effects. Alternative control algorithms, dependent on acquisition information other than the DR, might allow for improved yield and/or data quality.

Table E.1 Default acquisition parameters for LCC 4.2

Default algorithms	1	2	3	4	5	6
Name	Standard	Soft turn-on	Free running	Low detection rate	Interface low rate	Fast slew
Evaporation rate moving average filter depth (pulses)	10,000	10,000	10,000	50,000	50,000	10,000
Minimum DR (%)	0.5	0.5	0.5	0.1	0.1	0.5
Pulses per voltage update	5,000	10,000	10,000	25,000	25,000	5,000
At 200 kHz	$\frac{1}{40}$ s	$\frac{1}{20}$ s	$\frac{1}{20}$ s	$\frac{1}{9}$ s	$\frac{1}{9}$ s	$\frac{1}{40}$ s
Proportional coefficient (%/%)	−10.0	−0.1	−0.05	−0.1	−0.2	−10.0
Max upward voltage step (V)	0.5	1	5	2.5	2.5	1
At 200 kHz	20 V/s	40 V/s	200 V/s	100 V/s	100 V/s	40 V/s
Max downward voltage step (V)	0.5	1,000	1,000	1,000	1,000	1
At 200 kHz	20 V/s	40,000 V/s	40,000 V/s	40,000 V/s	40,000 V/s	40 V/s

Interface Evaporation Control Algorithm

Over time, the LEAP acquisition control algorithm has evolved to include a fast response feature termed interface evaporation control (IEC) that has demonstrated yield benefit for some sample types. The goal is to detect abnormal detection statistics (a possible signal preceding specimen failure) and minimize the chances for failure by quickly lowering the evaporation rate. It is difficult to rapidly change the specimen voltage due to the relatively high capacitance of the specimen stage and HV power supply, so schemes were developed to rapidly stop the applied pulse to the tip. The original implementation in software calculated an average DR over a pulse window (defined by the user). When the average rate exceeded the target rate by some factor, defined by the user, the software would stop firing of the voltage pulser (or deflect the laser off the tip) and lower the voltage by some amount (also defined by the user). Although the response of this algorithm is relatively quick compared to the control algorithm, a firmware implementation is significantly faster. Note that not all LEAP tools have the firmware implementation option.

The modern implementation of the IEC in LCC 4.2 uses the firmware to monitor ions emitted during consecutive pulses and responds immediately (voltage pulse generation is interrupted or laser pulse picking terminates, and the standing voltage is lowered prior to the next pulse). The user selects the sensitivity of the response (low, medium, or high), so when an extreme number of consecutive instrument pulses result in a detected ion (36 out of 40 pulses, 18 out of 20 pulses, or 9 out of 10 pulses, respectively) the instrument immediately lowers the voltage by an amount defined by the user. For typical target DRs (1 % or 1 ion for every 100 pulses) it is statistically unlikely for this sequence of detected events to occur randomly and indicates initiation of rapid tip change (the odds are less than 10^{-67}, 10^{-33}, and 10^{-17} for low, medium and high IEC, respectively). Quickly stopping this behavior should improve the chances for specimen survival for a wide variety of sample types. The occurrence of an IEC event is illustrated in Fig. E.5 by the large plus sign positioned immediately following the lowering of voltage which results in a correlated drop in DR. IEC settings are sample type specific, and a too sensitive setting will result in a lower average detection rate and a degraded signal-to-noise ratio (SNR).

Constant Flux Control

Keeping DR constant by manipulating only the voltage may not provide for the best yield or data quality. For example, background counts resulting from the field evaporation of adsorbed vacuum contaminants should be a function of DR, apex surface area, and pulse rate. Consequently, background levels might be improved by operating under constant evaporation flux (ion detection rate per unit area) rather

than DR (ion detection per time) [6]. For material systems that rarely fail during analysis, constant ion flux likely provides for a better SNR, more consistent evaporation physics, and possibly improved spatial reconstructions. In order to estimate the ion flux from the surface, an estimate of the specimen surface area is necessary. LCC allows the operator to enter an estimated evaporation field that it then uses with the specimen voltage to estimate surface area (see Chap. 5).

There is some danger or added complexity in implementing a constant flux control for inhomogeneous materials, especially for multilayer systems. First, relative to the constant DR algorithm, the electric field will be higher in order to increase the DR as emission area increases. This increases the chance of specimen failure as the analysis proceeds. Second, flux estimates are complicated for materials with differing evaporation fields present in the field of view simultaneously. Underestimating flux would again result in higher DRs, higher applied field, and higher likelihood of specimen failure. Finally, for multilayer systems, proceeding from a layer of low-field material to high-field material for example, the increasing specimen voltage necessary for evaporation of the high-field material may be incorrectly interpreted by a constant flux algorithm as an increase in emission area. The algorithmic demand for voltage (field) increase will be twofold: Constant flux requires the DR to be increased because of a perceived increase in emission area (increase in applied voltage), and the increasing field required by the material requires higher field (increase in applied voltage) to maintain even a steady DR. The combination of these two demands for increased field (voltage) increases likelihood of fracture, so any implementation of this type of algorithm must be considered carefully.

Constant Charge-State-Ratio Control

For pulsed laser acquisition, constant apex field/temperature is desirable for high data quality based on reasoning similar to that for constant flux. This type of control requires an ability to monitor the apex temperature and an algorithm to interpret this variable in order to modify pulse energy during acquisition. Because the evaporation field required to reach a particular rate is a function of temperature, charge-state ratios (CSRs) can provide an indirect indication of apex temperature [7]. The sensitivity of any given CSR to the actual temperature (at the time of evaporation) depends on the details of that particular ion species (rate of CSR change per rate of field change) and its response as a function of temperature (rate of field change as a function of temperature). A variety of theoretical and experimental behaviors have been observed [8, 9]. Implementation of such an algorithm might be straightforward because the DR could be controlled by voltage and the laser pulse energy could be controlled by CSR, so both controls are separate and decoupled; however, some of the same dangers recognized for constant ion flux exist for constant CSR mode applied to inhomogeneous systems. The particular ion species used to control laser pulse energy needs to be present everywhere in the specimen; otherwise,

sufficient conditional alternatives need to be in place to transition from one set of control criteria to another. In addition, the calibration file must be of sufficient quality to allow accurate interpretation of the mass spectrum during acquisition as a function of voltage.

Laser Positioning Control

The LEAP is designed to deliver maximum LPE density to the tip apex by utilizing a diffraction-limited laser spot (see Chap. 3) [10]. This approach avoids heating unnecessary regions of the tip and optimizes heat transfer from the apex to the bulk, thereby improving mass resolving power [10, 11]. This approach however is not without design challenges. The small spot size requires accurate targeting of the laser to the apex—as the specimen moves, the laser must follow, and when the laser moves or drifts it must be promptly repositioned back to the specimen apex. This coordinated alignment is susceptible to various instrumental instabilities which might include thermal expansion or contraction of various elements comprising the laser path, positioning optics, specimen, or specimen stage and can cause the laser position and/or apex position to drift on the order of a micron to a few microns during a multi-hour acquisition. Sub-micrometer repositioning corrections are required to keep the laser optimally aligned to the tip. A set of laser scanning algorithms are available and designed for periodic tracking of the laser spot to the tip apex as determined by the maximum observed DR.

Three scanning types are defined and can be modified by the user: Scout, Standard, and Drift Comp scans (see Table E.2). The Scout scan is intended to sweep large areas around a specimen to allow initial alignment of the laser spot to the specimen apex. For the LCC 4.2, a 12×12 μm^2 scanning area with 0.4 μm resolution is a practical limit to the scan size. The number of points in any scan is limited, and scanning with resolutions coarser than 0.4 μm risks missing detection of the maximum entirely. The Standard scan is intended to more accurately place the laser at the maximum detection position by utilizing a smaller scanning area which allows for finer scan resolution. Here the scan area is intended to include the entire area over which emission from the specimen can be observed and is a function of the actual tip dimensions coupled with the laser spot size. The overall dimensions of this scan can vary as a function of specimen type, DR, and LPE, and

Table E.2 Default scans defined for LCC 4.2 (see Appendix H of the *LEAP User Manual* for instrument-specific details on peak finding, thresholds, dwell time, and other laser scan information)

Laser position scans (μm)	Scout	Standard	Drift Comp
Tip scan edge size	12	1.2	0.25
Tip scan step size	0.4	0.12	0.025
Focus scan depth	20	10	3
Focus scan step size	4	2	1

so some adjustment to the default settings may be warranted by the user. The Drift Comp scan is intended for use during stable acquisition. In this mode only small corrections in laser position are necessary, and it is not desirable to allow the DR to be significantly reduced (any rate reduction likely causes a relative increase in signal background); hence, the drift scan covers only a small scan area. Similar to the Standard scan, the area over which the data rate is observed to change noticeably is specimen dependent, and so some tailoring of the scan range to specimen type may be warranted. A simple guideline is for the Drift Comp scan edges (corners) to dip to not more than ~50 % of the target DR and for the number of scan steps to fall between 25 and 100 (5 × 5–10 × 10 array steps). The control algorithm adjusts the dwell time for each step to attempt to ensure adequate counting statistics, so at low DRs, scan times can become significant.

Besides coordination of the lateral laser position with the specimen apex, the small focus depth of the laser requires coordination of the laser focus with the specimen apex as well. The elongated depth of focus reduces the relative sensitivity to motion along this direction, and so the correction is less significant. For LEAP 3000X systems, a focus correction at the beginning of an analysis may not need significant correction for many hours. LEAP 4000X systems have a lesser depth of focus requiring more frequent focus corrections (~hourly).

Also shown in Table E.2 are the default settings for the LCC 4.2 Scout, Standard, and Drift Comp focus scans. The Scout focus scan is intended to cover a wide range of focus depth using the Scout aerial scan and might only be needed after a local electrode change when the required position of the laser focus changes significantly. The Standard focus scan uses the Standard aerial scan and is intended to cover a more narrow range of focus depth. The Standard focus scan is suggested as an initial scan at the beginning of an analysis that has significant and stable ion emission. The Drift focus scan uses the Drift aerial scan and is intended to be quick and provide only small adjustments to the laser focus position. This is the scan that is used during automated acquisition. Note that not all materials run well under default automated focus scan conditions.

Two notable features exist to aid the performance of the tip tracking algorithm: *Mass Filter Ranges* and *Extended Dwell Time* are both defined on the LCC Advanced Controls tab within the Laser Atom Probe tab. When scanning over a specimen, a variety of emitted ion types can be observed. The goal of proper tip tracking is for the laser to be positioned in the place that results in maximum in-time specimen ion emission. Depending on the specimen structure, there may be places on the specimen that will emit ions at greater intensities but are dominated by out-of-synch or adsorbed ion species (the platinum weld on a lift-out specimen for example). To avoid this, the user can define up to three ranges to use for calculating DR during a laser scan. Default ranges exclude hydrogen and water ion peaks. The *Extended Dwell Time* check box allows the user to triple the amount of time devoted to individual laser steps. This may be necessary when scan statistics at low DRs are insufficient to result in acceptable tip scanning. All of the user-selected features on the Advanced Control tab can be saved, enabling customized scan sizes for various specimen classes.

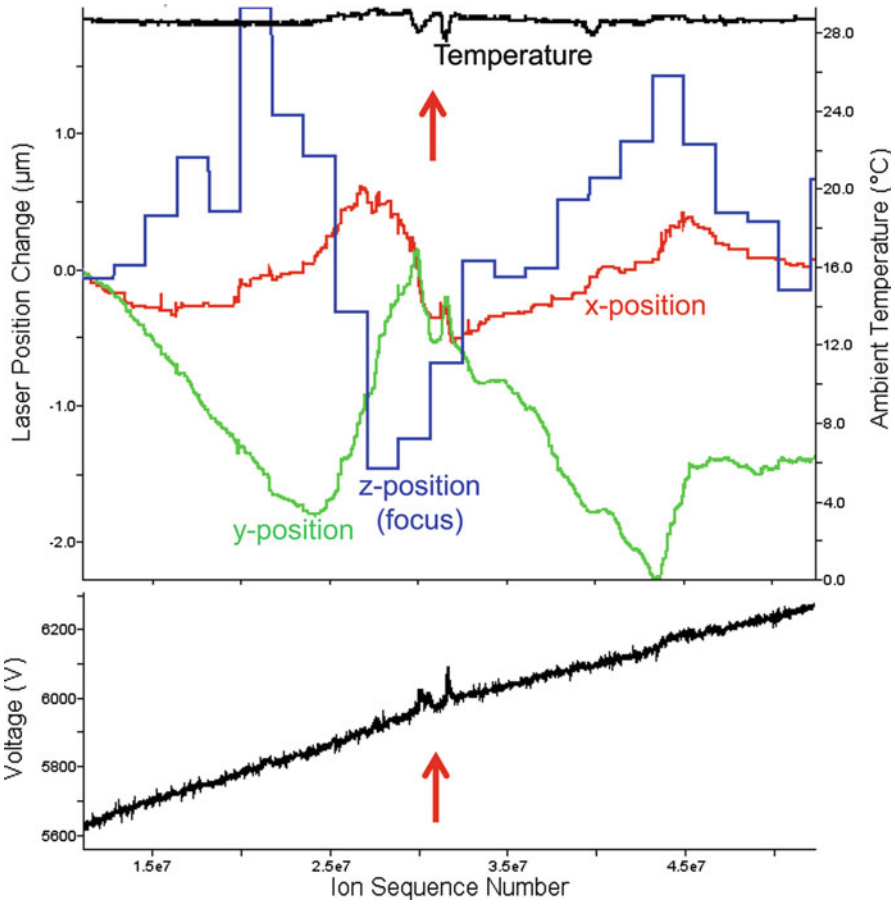

Fig. E.6 IVAS Wizard plot of laser position and ambient temperature for a 24-h microtip run (*top*). The laser scanning frequency and size were insufficient to compensate for an external temperature variation that occurred during the middle of the analysis (indicated by the accompanying rise in voltage—*bottom plot*). Higher scan frequency or larger area may be warranted. Hourly focus scans reveal changes in focus of up to 1.5 µm, and these are correlated to large lateral laser shifts as well. For the 4000X, 1 µm focus changes are significant. More frequent focus scans may be warranted in this example

In order to assess laser tracking stability, it is suggested to monitor laser position over the course of a long analysis (silicon microtip analyzed overnight for example) during which regular lateral and focus scans are performed. Any unexplained excursions in the voltage plot (not attributable to normal evolution due to changes in specimen composition and structure) may be a sign of poor laser tracking. Using the Cal/Recon Wizard step 2 in IVAS (see Chap. 5), a Laser Pos. and Ambient Temp. Hist. plot is available that shows laser position change vs. ion sequence number (Fig. E.6). Analysis of this plot should allow for sensible scanning frequency adjustments to be made.

References

1. Lunger, M.J., Vergason, G.E.: Reducing pump-down time with dry air venting. Soc of Vacuum Coaters 43rd Annual Technical Conference Proceedings, p 432 (2000)
2. Dylla, H.F., Manos, D.M., Lamarche, P.H.: Correlation of outgassing of stainless-steel and aluminum with various surface treatments. J. Vac. Sci. Tech. **11**(5), 2623–2636 (1993), DOI:10.1116/1.578617
3. Fowler, R.H., Nordhiem, L.: Electron emission in intense electric fields. Paper presented at the Proceedings of the Royal Society of London. Series A, Containing Papers of a Mathematical and Physical Character
4. Miller, M.K.: Atom Probe Tomography: Analysis at the Atomic Level. Kluwer Academic/Plenum Publishers, New York, NY (2000)
5. Li, Y., Ang, K.H., Chong, G.C.Y.: Patents, software and hardware for PID control - an overview and analysis of the current art. IEEE Contr. Syst. Mag. **26**(1), 42–54 (2006)
6. Gault, B., Moody, M.P., Cairney, J.M., Ringer, S.P.: Atom Probe Microscopy. Springer Series in Materials Science, vol. 160. Springer (2012)
7. Kingham, D.R.: The post-ionization of field evaporated ions: a theoretical explanation of multiple charge states. Surf. Sci. **116**, 273–301 (1982)
8. Tsong, T.T.: Field ion image formation. Surf. Sci. **70**, 211–233 (1978)
9. Southworth, H.N., Ralph, B.: J. Microsc., 90 (1969)
10. Bunton, J.H., Olson, J.D., Lenz, D.R., Larson, D.J., Kelly, T.F.: Optimized laser thermal pulsing of atom probe tomography: LEAP 4000X. Microsc. Microanal. **16**(Suppl 2), 10–11 (2010)
11. Bunton, J.H., Olson, J.D., Lenz, D.R., Kelly, T.F.: Advances in pulsed-laser atom probe: instrument and specimen design for optimum performance. Microsc. Microanal. **13**, 418–427 (2007)

Glossary

1D 2D 3D The dimensionality of data. 1D refers to a one-dimensional analysis such as a mass histogram or a 1D concentration profile. 2D refers to a two-dimensional dataset where the data lie in a single plane, such as a hitmap or a picture. 3D refers to a three-dimensional analysis, such as a position file.

1DAP 3DAP 1D or 3D atom probe instruments. 3DAP was also the model name of an instrument produced by Oxford Nano Science.

AMETEK AMETEK, Inc is a global manufacturer of electronic instruments and electromechanical devices with headquarters in the United States and over 80 manufacturing sites worldwide. CAMECA SAS is part of AMETEK's Materials Analysis Division.

Amplifier time-to-digital converter (ATDC) A time-to-digital converter that records the time of occurrence of independent electrical pulse inputs, each measured relative to a single, common reference input. It records timing events from each side of the three DLD anodes.

Analysis chamber The vacuum chamber in which specimens are analyzed in the LEAP.

Annular milling A type of FIB milling pattern.

Aperture The opening in a local electrode through which ions pass after evaporating from the specimen tip.

Appm Atomic part per million.

APT See atom probe tomography.

ASCII American standard code for information interchange.

ATDC See amplifier time-to-digital converter.

ATO A file format containing the same information contained in a POS file with additional data such as raw time of flight and other information used in data reconstruction.

Atom probe tomography (APT) The subject of this handbook. Please read the entire handbook for more information.

D.J. Larson et al., *Local Electrode Atom Probe Tomography: A User's Guide*,
DOI 10.1007/978-1-4614-8721-0, © Springer Science+Business Media New York 2013

Background Recorded event in the mass spectrum which do not originate from the specimen or are not found within a peak (not correlated to a voltage or a laser pulse).

Backside Specimen preparation orientation such that the analysis proceeds from below the original surface and toward the exposed surface (opposite of top-side or top-down analysis).

Bakeout The process of heating the LEAP instrument to approximately 150 °C. A bakeout is performed after the LEAP vacuum chambers have been exposed to air and assists in achieving high or ultrahigh vacuum.

Base pressure The standard operating pressure within a particular vacuum chamber in the LEAP instrument.

BCC Body-centered cubic.

Bgd See background.

Bias voltage The DC voltage applied to the specimen during data acquisition.

Bowl correction A time-of-flight correction to retain the relationship that all ions of the same mass and charge record the same time flight for all locations on the detector.

Buffer chamber A vacuum chamber between the load-lock and analysis chambers. This is the second of two chambers in which a carousel may be located and the chamber from which specimen and local electrode pucks are stored for use.

Calibration specimen A standard specimen (often aluminum or doped silicon) that produces consistent data quality when the LEAP system is operating properly such that it can be used to monitor system performance.

CAMECA ROOT A software application developed within the framework of ROOT, a Lesser General Public License object-oriented framework for data analysis developed by the European organization CERN.

CAMECA SAS A company based in Gennevilliers, France, that produces scientific instrumentation including SIMS, EPMA, LEXES, and APT. CAMECA was originally an acronym for *Compagnie des Applications Mécaniques et Electroniques au Cinéma* et à *l'Atomistique* but has been out of the film business since the late 1960s. It has several subsidiaries, including CAMECA Instruments, Inc., Madison, WI-based headquarters for CAMECA in North America.

Capping Deposition of sacrificial material on top of a sample to protect it during specimen preparation.

Carousel A carousel is a platter onto which is loaded either local electrode pucks or specimen pucks. The carousel resides in the load-lock or storage chamber.

Carousel heater An optional load-lock upgrade that enables baking of local electrodes and/or specimens in the load-lock chamber to rapidly degas them.

CERN Conseil Européen Pour La Recherche Nucléaire, now referred to as the European Laboratory for Particle Physics.

Client PC A desktop computer loaded with the LCC software through which a LEAP system operator controls LEAP functions such as data acquisition, specimen-to-local electrode alignment, and ISdb functions.

Co-evaporation When multiple ions evaporate from the specimen during a single pulse.

Cold finger The part of the cryostat at which refrigeration is concentrated. The cold finger is mechanically isolated from the specimen stage to reduce specimen vibration during data acquisition. It is thermally connected to the specimen stage by thermally conductive helium gas.

Complex ion An ion that contains more than one atom, also known as a molecular ion.

Constant CSR A data collection mode where the laser power control algorithm calculates and maintains a constant CSR for a species in the specimen.

Constant flux A data collection mode where the specimen voltage control algorithm calculates and maintains a constant ion/nm^2/s detection rate.

Cross Section Refers to preparing a specimen such that the analysis proceeds parallel to the original exposed surface (also known as parallel orientation).

Cryogenic temperature controller This device, located in the Instrument rack, controls the temperature of the cold finger that cools the specimen. The cold finger has a constant cooling power; the cryogenic temperature controller adds heat to the cold path with a resistive coil to regulate temperature.

CSR Charge-state ratio.

Da Dalton—the SI atomic mass unit (AMU).

Data acquisition See atom probe analysis.

DAVis Data acquisition and visualization system. The LEAP software component that provides 2D, digital specimen analysis data to the workstation. This software also provides run-time mass spectra and monitors specimen voltage, ion detection rates, etc.

Delay line detector A PSD designed to provide high-speed resolution of the time of flight and XY-coordinate encoding of a single or multiple ions. The DLD consists of serpentine DLAs and timing circuits. A charge cloud produced by the microchannel plates impinges on the DLD creating an electromagnetic pulse that travels each direction to the ends of the delay line and out to the ATDC timing circuits.

Delocalization A smoothing function allowing discrete data produced by the LEAP to create the 3D concentration grid used to create surfaces in IVAS.

Deprocessing A specimen preparation step where unwanted regions are removed from near the region of interest. Often used when preparing microelectronic samples.

Desiccant A drying agent typically used in dry-box applications to prevent moisture from accumulating on local electrodes and specimens in storage. Only dust-free desiccants are recommended for local electrode storage.

Desorption Field evaporation of gas ions adsorbed onto the specimen surface.

Detector A device within the LEAP instrument that includes the MCP and DLD and which detects ions released during data acquisition.

Detector space A coordinate system based on the curved specimen surface projected onto the flat detector and is displayed in live time in DAVis. Detector

space is visualized in a real space reconstruction as hemispheres centered on the reconstruction center.

Discrete discrimination The ability to discern the identity of each individual ion in a dataset, which can be complicated by high background noise or a small peak in the tail of a large peak.

DLA Delay line anode.

DLD See delay line detector.

DR Detection rate.

Dry box A storage device specifically designed to maintain a moisture-free environment for electrodes and specimens.

EDS Energy-dispersive X-ray spectroscopy (also known as EDX).

EDX Energy-dispersive X-ray spectroscopy (also known as EDS).

Electric field The distribution in space of the strength and direction of the force that would be exerted on an electric charge at any point in that space. Units for APT are typically V/nm.

Electrode See local electrode.

Electropointer™ A motorized electropolishing system with automatic and manual modes (produced by Simplex Scientific)™.

Electropolishing The process of applying a positive charge to a sample while immersed in an electrolyte in order to remove material and sharpen the sample into a specimen.

ENV The environment file used in TAP instruments that contains ranging and reconstruction information.

ePOS The extended POS file containing the information in the POS file and additional data such as raw time of flight and other information used in data reconstruction.

ESD Electrostatic discharge.

Evaporation See field evaporation.

Experiment See atom probe analysis.

FCC Face-centered cubic.

FEEM Field electron emission microscopy.

FET Field effect transistor.

FFT Fast Fourier transform.

FIB See focused ion beam.

FIB-LO Focused ion beam lift-out. The process of making APT specimens with an FIB.

Field enhancement Increase in electric field due to the proximity of the local electrode to the specimen.

Field evaporation The phenomena that results in specimen atoms being ionized in the presence of extremely high electric field of the order of a few to tens of V/nm.

Field ion microscopy The process where gas atoms adsorbed on the tip of a specimen are ionized by a high electric, becoming positively charged, and are

repelled from the tip. The curvature of the surface near the tip causes a natural magnification—ions are repelled in a direction roughly perpendicular to the surface, producing a "point projection" effect. A DLD or a phosphor screen is used to visualize the ions.

FIM See field ion microscopy.

Flash See specimen fracture.

Flat-test The procedure to test the quality of a local electrode.

Flat-top microtip array A silicon coupon with an array of blunt-topped specimen posts. These coupons provide an efficient way to do precise and accurate FIB lift-out specimen preparation techniques.

Flight path The space inside the atom probe that ions pass through when they leave the specimen and travel to the detector.

Focused ion beam A specimen preparation and milling technique typically using gallium as the focused ion medium to micro-machine samples into specimens.

FOV Field of view.

Fracture See specimen fracture.

FW0.01M Full width 1/100th max—a measure of a spectral peak width or mass resolving power.

FW0.1M Full width 1/10th max—a measure of a spectral peak width or mass resolving power.

FWHM Full width half max—a measure of a spectral peak width or mass resolving power.

HAADF High-angle annular dark field—an imaging technique and detector type used in TEM.

Hit event A hit event is a per-pulse detection of an ion on any of the detector channels in the LEAP microscope.

Horizontal transfer rod The manually operated, magnetically coupled, horizontal rod that moves a specimen or a local electrode puck from the carousel in the buffer chamber to the analysis chamber.

HR The LEAP model including the large-angle reflectron flight path.

HVAC Heating, ventilation, and air conditioning.

IEC See interface evaporation control.

Image correction factor A variable in a large field-of-view reconstruction to correct for the fact that ions off of the center of the specimen apex do not travel in straight lines toward the detector, but rather ions leaving from locations closer to the specimen shank are increasingly compressed toward the center of the specimen apex.

Imago The proper noun for, and an acceptable truncation of, Imago Scientific Instruments Corporation. Acquired by AMETEK, Inc. Imago is now part of CAMECA Instruments, Inc.

Instrument flange The front flange on the LEAP instrument Analysis chamber, upon which is mounted the specimen stage, detector, pulser electronics, etc.

Instrument rack A rolling rack containing the LEAP microscope component computers, controllers, power supplies, a backup power system, and emergency system-power-cutoff switch.

Integrated scientific database See ISdb.

Integrated visualization and analysis software See IVAS.

Interface evaporation control A LEAP instrument feature that automatically and rapidly reduces field ionization when detection rate increases beyond a specified threshold to help reduce the incidence of specimen fracture.

Ion gauge A gauge that measures pressure in a vacuum chamber. The Instrument rack contains an ion gauge controller that converts the analog pressures into digital readouts.

ISdb™ The LEAP software component integrated into the LCC control system that queries, and updates, the specimen database. ISdb keeps track of locations and conditions of specimens and local electrodes as well as records experimental setup information. A trademark of CAMECA Instruments, Inc.

ITRS International technology roadmap for semiconductors.

IVAS Integrated visualization and analysis software. The LEAP software component that reconstructs specimen data into three-dimensional images and is used for data analysis. It is based on Java and Netbeans.

***k*-factor** A geometry-driven electric field enhancement factor used in reconstruction calculations.

LAR Large-angle reflectron. A specially designed electrostatic mirror for ions. It uses an electric field to reflect incoming ions from a specimen toward a detector. In the process, the reflectron improves mass resolving power by time-focusing ions of different energy onto the detector. With a LAR, it is possible to record a large field of view while maintaining high mass resolution.

LAS LEAP acquisition server. The LEAP software component through which acquisition commands are sent and that transfers acquisition data to the client PC.

Laser head Mode-locked laser cavity which produces pulses at a rate of 80 MHz with a fixed pulse energy.

Laser scan A process of rastering the laser beam over the specimen apex while monitoring the DR to identify the optimal laser spot location on the specimen apex.

LAWATAP Laser-assisted wide-angle tomographic atom probe. A previous generation of a 3D straight flight path atom probe.

LCC LEAP control center. The primary software user interface that controls the LEAP microscope.

LEAP Local-electrode atom probe. A proper noun for, and abbreviation of, the LEAP microscope. See LEAP Microscope.

LEAP acquisition server See LAS.

LEAP control center See LCC.

LEAP microscope The part of the LEAP system that is mounted on a chassis, contains vacuum chambers and other equipment and instruments, and from which specimen data originates. A CAMECA product designed to analyze specimens at the atomic scale.

LEAP system schematic The LEAP system schematic is a digital, pictorial, user interface in the LCC software representing the functions and features of the LEAP microscope, from which parts of the microscope are controlled.

LEAP system server See LSS.

LEAPnet A LEAP ethernet network that allows the workstation to communicate with the instrument-rack PC, which, in turn, communicates with other instruments in both the rack and on the LEAP instrument.

Load-lock chamber This chamber is the chamber into which you place carousels and is the first step in loading specimens and local electrodes into the instrument.

Local electrode The cone-shaped piece of metal mounted on a puck and positioned directly opposite the specimen in the analysis chamber. A brief, high-voltage pulse, supplied by the high-voltage pulser, which is applied to the local electrode during a voltage pulsed atom probe experiment. The local electrode improves the mass resolution, field of view, and acquisition speed of atom probe analysis and simplifies specimen preparation for atom probe analysis.

Local electrode puck The local electrode puck provides a mounting surface for the local electrode within the LEAP instrument. See Local Electrode.

LPE Laser pulse energy.

LPS Laser positioning server. The LEAP software component that controls laser position.

LSS LEAP system server. The LEAP software component that allows all LEAP software and components to communicate and interact.

m*/*n Mass-to-charge-state ratio, also expressed as m/c, m/e, m/q, m/z, and u/e.

Mass-to-charge-state ratio The mass-to-charge-state ratio of an ion is the ion's mass (in mass units) divided by its charge state (in charge units). The mass-to-charge-state ratio is on the x-axis of a mass spectrum and is indicated in SI units of Daltons (Da).

MCP See microchannel plate.

Metadata Metadata is information a user enters into a database and that can be used for sorting and searching the database. Adding specimens to the ISdb often requires adding to the database metadata about the specimen.

Microchannel plate Part of the atom probe detector system. The MCP is a transducer/amplifier that amplifies a single, charged species by approximately 1×10^6. Gain is controlled by the voltage difference between the front and back plate.

Microchannel plate amplifier See microchannel plate.

Micro-positioning stage controller An electronic component in the instrument rack that controls the micro-positioning motors in the specimen stage. These motors move the specimen relative to the fixed position of the local electrode.

Microtip array One of the two primary specimen-mounting geometries in preparing specimens for analysis. Microtip array coupons are ~3 × 7 mm^2 chips of silicon with an array of approximately 150 μm tall microtips etched on the surface. A trademark of CAMECA Instruments, Inc.

MRP Mass resolving power. A measure of the spectral quality of a peak in the mass-to-charge-state ratio histogram.

Multi-hit event A multi-hit event is the detection of two or more independent ions on the detector in the LEAP microscope.

Parallel-orientation analysis Refers to preparing a specimen such that the analysis proceeds across the surface of the original exposed surface (also known as cross-section orientation analysis).

Peak overlap The superposition of two peaks in a histogram. Si-28^{+} and Fe-56^{2+} for example.

PEEK Polyether ether ketone.

PF Pulse fraction.

Pixel The smallest addressable picture element in a display device.

PLAP Pulsed laser atom probe.

Plasma cleaner An optional hardware upgrade, the plasma cleaner is used to treat local electrodes which have been in storage for an extended period of time and to recover local electrodes which have failed due to specimen fracture.

POS A data file type consisting of the reconstructed ion position (x, y, z) and the mass-to-charge ratio for each reconstructed ion.

PoSAP Position-sensitive atom probe. It is also the software that was developed by Oxford Nano Science for use with the 3DAP instrument.

Puck A small carrier unit (~3 cm long) for specimens and local electrodes. These are mounted into a carousel to be transferred to the specimen stage in the analysis chamber.

Pulse generator A device that generates the electrical pulse delivered to the local electrode to ionize atoms from a specimen apex for voltage pulsed data acquisition.

Pulser See high-voltage pulser.

Ranging The process of identifying all the peaks in the mass-to-charge-state ratio histogram and choosing lower and upper bounds.

Reconstruction The process of turning the timing signals from the DLD into real space positions and identified ions.

Reflectron A specially designed electrostatic mirror for ions. It uses an electric field to reflect incoming ions from a specimen toward a detector.

Residual gas analyzer An optional LEAP instrument that measures the concentrations of gases within the analysis chamber.

RGA See residual gas analyzer.

RHIT A raw data file created by the LEAP that the user analyzes with IVAS.

ROI Region of interest: The region of special interest for analysis.

ROOT See CAMECA ROOT.

Roughing pump Roughing pumps are mechanical pumps for initial pumping of the load-lock and buffer chambers. Roughing pumps are required before applying the turbo pumps, the latter capable of achieving ultrahigh vacuum (UHV).

RRAW The raw data file: RRAW files contain the raw detector data and the order of ion collection from the LEAP as well as the history of various parameters measured or controlled throughout the acquisition.

RRNG ASCII format files that describe how mass ranges are associated with particular ion types.

Sample A sample is a representative part or a single item from a larger whole or group. For example, a sample is obtained from a wafer, and a specimen is prepared from a sample.

Sampling Taking a random subset of the collected information to increase calculation or display speeds. Typically, reconstruction calculations and charts in the IVAS wizard are limited to 500,000 ions or fewer.

SDM Spatial distribution map.

Shank angle A measure of specimen taper.

SIMS Secondary ion mass spectrometry.

Site specific Specimen preparation that targets a specific ROI.

SNR Signal-to-noise ratio.

Specimen The needle-shaped object of interest from which the LEAP microscope attains an image.

Specimen analysis See atom probe analysis.

Specimen database A LEAP software component where all specimens, local electrodes, and run conditions are recorded. See ISdb.

Specimen DB See ISdb.

Specimen failure See specimen fracture.

Specimen fracture A specimen fracture occurs when a specimen mechanically fails. Many common terms have been invented to describe failure including flash, rupture, failure, or zot.

Specimen puck See puck.

Specimen stage That part of the LEAP hardware, located inside the analysis chamber and part of the Instrument flange assembly, to which specimen and local electrode pucks are mounted.

Specimen stage controller See micro-positioning stage controller.

SRM Standard reference material.

Stage controller See micro-positioning stage controller.

Storage chamber See buffer chamber.

STR STR files contain the raw detector data and the order of ion collection from the LEAP as well as the history of various parameters measured or controlled throughout the acquisition. They are used in the latest LEAP systems to create RHIT files.

Stub A tube of metal, usually copper or nickel, which can accept wire geometry specimens and can be secured in a specimen puck. Also known as crimps or tubes.

TDC See amplifier time-to-digital converter.

Time of flight A mass spectrometry method for determining ion mass by measuring the time it takes to travel a known distance.

Tip tracking A LEAP run mode where the laser position control algorithm maintains the laser position in the optimal location over the specimen apex.

TMP See turbo pump.

TODS Time of departure spread.

TOF See time of flight.

Top down Refers to specimen preparation where analysis proceeds from the original exposed surface into the sample (it is also known as normal orientation and is the opposite of backside sample preparation).

Torr A unit of pressure equal to 1/760 of an atmosphere or about 133.3 Pa or 1.333×10^{-3} bar. The primary unit of measuring pressure in the vacuum chambers of the LEAP instrument.

Trajectory aberrations Any effect that causes ions leaving the surface to travel toward the detector in unexpected paths.

Turbo pump Turbomolecular pump. One of several vacuum pumps on the LEAP system that helps the LEAP vacuum chambers achieve ultrahigh vacuum.

Turn-on A phrase referring to the onset of emission (either electron or ion emission).

UHV Ultrahigh vacuum. Any vacuum lower than 10^{-9} Torr.

UHV CLEAN A condition that indicates that the object is ready to be used in a UHV environment. It typically requires 3–5 cleaning steps, ending with several rinses, often in an ultrasonic bath, of high purity, low-moisture alcohol.

UHV foil An aluminum foil, applied as a dust cover to UHV clean parts. It is made without the use of manufacturing oils. UHV foil is the preferred foil for protectively wrapping UHV clean CAMECA LEAP microscope parts.

Unsampled The unsampled option displays all ions rather than a sampling of the entire dataset.

UV Ultraviolet

Vertical transfer rod The motor-driven (vertical motion), magnetically coupled vertical rod that moves a specimen or an local electrode puck between the carousel in the buffer chamber to the specimen stage in the analysis chamber.

Voltage correction A time-of-flight correction to retain the relationship that all ions of the same mass and charge record the same time of flight for all analysis voltages.

Voxel A volume or 3D pixel.

Workstation See client PC.

Yield Analysis yield is fraction of all APT measurements.

Index

D.J. Larson et al., *Local Electrode Atom Probe Tomography: A User's Guide*,
DOI 10.1007/978-1-4614-8721-0,